INFLUENCE OF TOPOGRAPHY AND SURFACE CHEMISTRY ON THE WETTING PROPERTIES OF TiO_2-BASED CERAMIC COATINGS

Mikael Järn

2010

Laboratory of Physical Chemistry

Department of Natural Sciences, Åbo Akademi University

Graduate School of Materials Research

Center for Functional Materials (FunMat)

Åbo, Finland

INFLUENCE OF TOPOGRAPHY AND SURFACE CHEMISTRY ON THE WETTING PROPERTIES OF TiO_2-BASED CERAMIC COATINGS

by

Mikael Järn

Åbo Akademi
University

2010

Laboratory of Physical Chemistry
Department of Natural Sciences, Åbo Akademi University
Graduate School of Materials Research
Center for Functional Materials (FunMat)
Åbo, Finland

From

Laboratory of Physical Chemistry
Department of Natural Sciences
Åbo Akademi University, Åbo, Finland

and

Graduate School of Materials Research (GSMR)
Åbo, Finland

Supervised by

Dr. Mika Lindén
Laboratory of Physical Chemistry
Department of Natural Sciences
Åbo Akademi University, Åbo, Finland

and

Prof. Jarl B. Rosenholm
Laboratory of Physical Chemistry
Department of Natural Sciences
Åbo Akademi University, Åbo, Finland

Reviewed by

Dr. Rossen Sedev
Ian Wark Research Institute
University of South Australia, Adelaide, Australia

and

Dr. Neil Shirtcliffe
School of Biomedical & Natural Sciences
Nottingham Trent University, Nottingham, UK

Dissertation Opponent

Dr. Rossen Sedev
Ian Wark Research Institute
University of South Australia, Adelaide, Australia

ISBN 978-952-12-2470-6
Painosalama Oy – Turku, Finland 2010

TABLE OF CONTENTS

PAPERS I-VI

ABSTRACT

The wetting properties of solids are important in many natural systems as well as in a wide range of technical applications. It is well-know that the wettability of a solid surface is governed by both the surface chemistry and the surface structure.

In this thesis, the wettability of TiO_2-based ceramic coatings was studied. The coatings were prepared by utilizing sol-gel dip-coating technology. In the first part of the thesis, one component TiO_2 coatings with random heterogeneities were studied. The topography of the coatings was varied by changing the synthesis conditions, e.g. calcination temperature and with the addition of additives. The topography of the coatings was described with a series of roughness parameters. It was shown that the often used root mean square roughness (RMS) is not sufficient enough to describe the topography of a surface. The influence of surface topography on the wetting properties was also studied. Furthermore, the combined effect of topography and surface wettability on the precipitation kinetics of calcium phosphate (CaP) on the coatings was investigated. It was found that a hydrophilic coating together with a specific surface structure is more favorable to initiate the formation of CaP. In the next step, strongly water-repellant coatings were prepared by the spontaneous formation of CaP followed by hydrophobization with a perfluorophosphate surfactant. The superhydrophobicity could be explained by the morphology of the coating, where the solid-liquid contact was minimized.

In the second part of the thesis, well-ordered nanopatterns of TiO_2 on silica or gold substrates were prepared with the evaporation induced self-assembly (EISA) technique. The material consists of a very thin layer of titania, where the substrate is accessible through hexagonally ordered nanocraters aligned perpendicularly to the surface. Such nanopatterned surfaces are ideal model systems for detailed wettability studies, since the titania network and the substrate (SiO_2 or Au) can be selectively functionalized with various organic molecules. The influence of the geometry (pore diameter, wall thickness, layer thickness) and hydrophilic-hydrophobic contrast on the wetting properties were studied. The experimental results could successfully be modeled with existing theories for the wetting of rough and heterogeneous surfaces.

LIST OF ORIGINAL PUBLICATIONS

I. **Topographical parameters for specifying a three-dimensional surface**
J. Peltonen, **M. Järn**, S. Areva, M. Lindén, J. B. Rosenholm, *Langmuir* **2004**, *20*, 9428-9431.

II. **Topography and surface energy dependent calcium phosphate formation on sol-gel derived TiO_2 coatings**
M. Järn, S. Areva, V. Pore, J. Peltonen, M. Lindén, *Langmuir* **2006**, *22*, 8209-8213.

III. **Bioinspired synthesis of superhydrophobic coatings**
M. Järn, M. Heikkilä, M. Lindén, *Langmuir* **2008**, 24, 10625-10628.

IV. **Surface nanopatterning by organic/inorganic self-assembly and selective local functionalization**
A. Fisher, M. Kuemmel, **M. Järn**, M. Lindén, C. Boissière, L. Nicole, C. Sanchez, D. Grosso, *Small* **2006**, *4*, 569-574.

V. **Wetting of heterogeneous nanopatterned inorganic surfaces**
M. Järn, F. Brieler, M. Kuemmel, D. Grosso, M. Lindén, *Chemistry of Materials* **2008**, *20*, 1476-1483.

VI. **Wetting studies of hydrophilic-hydrophobic TiO_2@SiO_2 nanopatterns prepared by photocatalytic decomposition**
M. Järn, Q. Xu, M. Lindén, *Langmuir* **2010,** *26*, 11330-11336.

LIST OF SUPPORTING PUBLICATIONS

1. M. Järn, B. Granqvist, J. Lindfors, T. Kallio, J. B. Rosenholm, A critical evaluation of the binary and ternary solid-oil-water and solid-water-oil interaction, *Adv. Colloid Interface Sci.* **2006**, *137*, 123-126.

2. M. Järn, C-M. Tåg, J. Järnström, B. Granqvist, J. B. Rosenholm, Alternative models for determining the surface energy components in offset printing, *J. Colloid Int. Sci* **2006**, *301*, 668-676.

3. J. Andersson, E. Johannessen, S. Areva, **M. Järn**, M. Linden, Wet powder processing of sol-gel derived mesoporous silica-hydroxyapatite hybrid powders, *J. Nanosci. Nanotechnol.* **2006**, *6*, 2438-2444.

4. B. Granqvist, M. **Järn,** J. B. Rosenholm, Critical Evaluation of the Surface Energy Components of solids, *Colloids and Surfaces A* **2007**, *296*, 248-263.

5. J. Järnström, B. Granqvist, **M. Järn**, C-M. Tåg, J. B. Rosenholm, Alternative methods to evaluate the surface energy components of ink-jet paper, *Colloids and Surfaces A* **2007**, *294*, 46-55.

6. V. Pore, M. Ritala, M. Leskelä, S. Areva, **M. Järn**, J. Järnström, H_2S modified atomic layer deposition process for photocatalytic TiO_2 thin films, *J. Mater. Chem*. **2007,** *17*, 1361-1371.

7. B. Granqvist, J. Järnström, C-M. Tåg, **M. Järn**, J. B. Rosenholm, Acid-Base properties of polymer coated papers, *J. Adhesion Sci. Technol.* **2007,** 21, No. 5-6, 465-485.

8. C-M. Tåg, **M. Järn**, B. Granqvist, J. Järnström, J. Peltonen, J. B. Rosenholm, The influence of surface structure on the wetting of coated offset papers, *Holzforschung* **2007**, *61*, 516-522.

9. M. Harju, J. Halme, **M. Järn**, J.B. Rosenholm, T. Mäntylä, Influence of aqueous aging on surface properties of plasma sprayed oxides, *J. Colloid. Int. Sci.* **2007,** *313(1)*, 194-201.

10. X. Zhang, M. Honkanen, **M. Järn**, J. Peltonen, V. Pore, E. Levänen, T. Mäntylä, Thermal Stability of Structural Features in the Superhydrophobic Boehmite films on Austenitic Stainless Steels, *Applied Surface Science* **2008**, *254*, 5129-5233.

11. M. Raulio, **M. Järn**, J. Ahola, J. Peltonen, J.B. Rosenholm, S. Tervakangas, J. Kolehmainen, T. Ruokolainen,P. Narko and M. Salkinoja-Salonen. Microbe repelling coated stainless steel analysed by field emission scanningelectron microscopy and physicochemical methods, *Journal of Industrial Microbiology and Biotechnology* **2008**, *35 (7)*, 751-760.

12. J-H. Smått, N. Schüwer, **M. Järn**, W. Lindner, M. Linden, Synthesis of Micrometer Sized Mesoporous Metal Oxide Spheres by Nanocasting, *Mesoporous and Microporous Materials* **2008**, *112*, 308-318.

13. X. Zhang, **M. Järn**, J. Peltonen, V. Pore, T. Vuorinen, E. Levänen, T. Mäntylä, Analysis of roughness parameters to specify superhydrophobic antireflective boehmite films by the sol-gel process, *Journal of the European Ceramic Society* **2008**, *28*, 2177-2181.

14. J-P. Nikkanen, H. Keskinen, M. Aromaa, **M. Järn**, T. Kanerva, E. Levänen, J. M. Mäkelä, T. Mäntylä. Iron Oxide Doped Alumina-Zirconia Nanoparticle Synthesis by Liquid

Flame Spray from Metal Organic Precursors, *Research Letters in Nanotechnology* **2008**, Available on the web. Article ID 516478, doi:10.1155/2008/516478

15. M. Harju, **M. Järn**, P, Dahlsten, J. B. Rosenholm, T. Mäntylä, Influence of long-term aqueous exposure on surface properties of plasma sprayed oxides Al_2O_3, TiO_2 and their mixture Al_2O_3-13TiO_2, *Applied Surface Science* **2008**, *254 (22),* 7272-7279.

16. M. Harju, **M. Järn**, P, Dahlsten, J-P. Nikkanen, J. B. Rosenholm, T. Mäntylä, Influence of long-term aqueous exposure on surface properties of plasma-sprayed oxides Cr_2O_3 and Cr_2O_3-25wt% TiO_2, *Journal of Colloid and Interface Science* **2008**, 326 (2), 403-410.

17. A. Leitner, M. Sturm, J.-H. Smått, **M. Järn**, M. Lindén, K. Mechtler, W. Lindner, Optimizing the performance of tin dioxide microspheres for phosphopeptide enrichment, *Analytica Chimica Acta* .638 (2009) 51-57

18. V. Pore, M. Ritala, M. Leskelä, T. Saukkonen, **M. Järn**, Explosive Crystallization in Atomic Layer Deposited Mixed Titanium Oxides, *Crystal Growth & Design* **2009**, *9 (7),* 2974-2978.

19. P. Pulkkinen, J. Shan, K. Leppänen, A. Känsäkoski, A. Laiho, **M. Järn**, H. Tenhu, Polyethylene imine and tetraethylene pentamine as protecting agents for metallic copper nanoparticles, *Applied Materials & Interfaces* **2009**, 1 (2), 519-525.

20. M. Järn, C-M. Tåg, J. Järnström, J. B. Rosenholm, Dynamic spreading of polar liquids on offset papers, *J. Adhesion Sci. Technol.* **2010,** *24*, 567-581.

21. C-M. Tåg, **M. Järn**, J. B. Rosenholm, Radial spreading of ink and model liquids on heterogeneous polar surfaces, *J. Adhesion Sci. Technol.* **2010,** *24*, 539-565.

CONTRIBUTION OF THE AUTHOR

The author is responsible for all the experimental work in the thesis with the following exceptions:

The TiO_2 coatings in Paper I-III were prepared by Dr. Sami Areva.

The XRD measurements in Paper II were conducted by Dr. Viljami Pore.

The XRD measurements in Paper III were conducted by M.Sc. Mikko Heikkilä.

The nanopatterned surfaces in Paper IV were prepared by Dr. Monica Kümmel.

The nanopatterned surfaces in Paper V were prepared by Dr. Monica Kümmel and Dr. Felix Brieler.

The nanopatterned surfaces in Paper VI were prepared by M.Sc. Qian Xu.

ABBREVIATIONS AND SYMBOLS

θ	Contact angle
ϕ	Interaction parameter
γ	Surface tension/energy
AB	Acid-base
AFM	Atomic force microscopy
CA	Contact angle
CaP	Calcium phosphate
CTAB	Cetyltrimethylammonium bromide
f	the projected area fraction
F	the 3D area fraction
HA	Hydroxyapatite
IEP	Isoelectric point
LW	Lifshitz-van der Waals
OCP	Octacalcium phosphate
PEG	Polyethylene glycol
r	Wenzel roughness value
RMS	Root-mean square
SAM	Self-assembled monolayer
SBF	Simulated bodyfluid
SPM	Scanning probe microscopy
STM	Scanning tunneling microscopy
SEM	Scanning electron microscopy
$TiO_2@SiO_2$	Titanium dioxide on silicon dioxide
$TiO_2@Au$	Titanium dioxide on gold
vOCG	van Oss, Chaudhury, Good
XPS	X-ray photoelectron spectroscopy
XRD	X-ray diffraction

1. INTRODUCTION AND OUTLINE

Wettability, i.e. how liquids behave on solids, is an important phenomenon in nature as well as in many technical applications. Wetting phenomena play an important role in for instance painting, coating, and printing industries, or when designing windshields, waterproof clothing, cosmetics etc.[1] On high-energy surfaces, most liquid droplets spread out on the surface in the form of a thin liquid film, while on a low-energy surface partial wetting occurs and most droplets form a spherical cap on the surface. The liquid/fluid interface meets the solid surface at an angle θ, called the contact angle, which is the measureable characteristic of a solid/liquid interface. A solid surface is defined as hydrophobic, when the contact angle of a water droplet is > 90°, or hydrophilic, when the contact angle is < 90°. By chemically modifying a flat surface, a maximum water contact angle of roughly 120° can be achieved. To achieve higher apparent contact angles, one needs to modify the structure of the surface.[2] This is something that nature effectively has taken advantage of. One classical example is the Lotus leaf, which exhibits so-called self-cleaning properties, seen as the removal of loosely adhered dust and dirt particles from the surface by rolling water droplets.[3] The rough surface structure together with the low surface energy results in the high water-repellency, also called superhydrophobicity.[1, 4] Other examples of superhydrophobic surfaces in nature are the legs of the water strider, the wings of butterflies, and duck feathers. With the inspiration from nature, during the last decade a lot of effort has been made in designing artificial superhydrophobic surfaces for various applications. A large number of different routes and materials have been used for the fabrication of such surfaces.[4] Properties like strength, toughness, hardness, flexibility, optical transparenncy, electrical conductivity etc. may be desired of the final material, and must therefore be taken into account when deciding on a suitable method of preparation. [4]

The surface structure can also be used to improve the wettability of a surface. For a hydrophilic surface ($\theta < 90°$), roughening of the surface structure generally leads to an improved wettability. This is one of the bases for the creation of superhydrophilic surfaces, which means that a water droplet fully spreads and forms a film on the surface.[5] If the surface is tilted, the liquid film flows off the surface, thus leading to another type of self-cleaning process.[2] The formation of a thin film of water is for example desired in the designing of antifogging surfaces.[6]

Titanium dioxide (TiO_2) is one of the most widely studied materials in relation to self-cleaning because of its photocatalytic activity. [7, 8] When TiO_2 is subjected to irradiation with energy greater than its band gap (3.0-3.2 eV), it has the ability to oxidize various organic compounds.[9, 10] Additionally, TiO_2 becomes strongly hydrophilic when subjected to UV irradiation, which has a positive effect on surface cleanability.[8] TiO_2 coatings are also biocompatible, and can therefore be used as dental or orthopedic implants.[11] Furthermore, TiO_2 coatings have both high mechanical and chemical stability and are fairly easy to prepare using various techniques. The TiO_2-based surfaces studied in this thesis were prepared using sol-gel dip-coating technology.

The outline of this doctoral thesis is to first review the literature on the wetting of rough and heterogeneous surfaces. In the "Materials and methods" section the synthesis of the TiO_2-based coatings is generally described. The most central surface characterization techniques are also described more in detail. The "Results and discussion" section can roughly be divided into two parts: *TiO_2 surfaces with random heterogeneity* (Paper I-III) and *Nanopatterned TiO_2 surfaces* (Paper IV-VI). The use of topographical roughness parameters for describing a series of randomly heterogeneous TiO_2 surfaces in three dimensions is demonstrated in Paper I. The combined effect of surface topography and surface chemistry of a series of TiO_2 coatings on calcium phosphate precipitation kinetics was further investigated in Paper II. The understanding of what parameters that control the formation of inorganic deposits is important within several fields. For example, in many industrial processes the formation of inorganic scales is a severe problem, while in bioapplications rapid nucleation and growth of calcium phosphates is often desired.[12]

In paper III, a simple bioinspired approach was utilized to prepare a superhydrophobic coating. The coating is self-organizing through the spontaneous formation of calcium phosphate on a TiO_2 substrate. The coating was hydrophobized with a perfluorophosphate surfactant.

Papers IV-VI deal with the preparation and characterization of well-ordered nanoperforated layers of TiO_2 on silicon wafers or gold-coated wafers. The material consists of a very thin layer of titania, where the substrate is accessible through hexagonally ordered nanocraters aligned perpendicularly to the surface. Such nanopatterned surfaces are ideal model systems for detailed wettability studies, since the titania network and the substrate (SiO_2 or Au) can be selectively functionalized with various organic molecules. The wettability of selectively functionalized TiO_2 on SiO_2 and TiO_2 on Au nanopatterns was studied in papers V and VI. The experimental results were also compared with existing theories for the wetting of rough and heterogeneous surfaces. The understanding of the wettability of nanostructured materials is important for applications within fields like microfluidics[13, 14] and sensing.[15]

2. BASIC WETTING MODELS

2.1. Ideal, smooth surfaces

2.1.1. The Young equation

The most common way to determine the surface energy of a solid surface is by measuring the contact angle, θ, of a probe liquid with known properties. The contact angle is defined as the angle between the tangent to the liquid-vapor interface and the tangent to the solid interface at the contact line between the three phases (Figure 1). The correlation between the contact angle and the interfacial tensions is known as the Young equation.[16]

$$\gamma_{SV} = \gamma_{LV} \cos\theta_Y + \gamma_{SL} \qquad (1)$$

where γ_{SV} is the solid-vapor interfacial energy, γ_{LV} the liquid-vapor interfacial tension, and γ_{SL} the solid-liquid interfacial energy. This equation was developed for an ideal solid surface, which is defined as smooth, rigid, chemically homogeneous, insoluble, and non-reactive. The Young contact angle θ_Y, is referred to as the ideal contact angle. For a real surface, the problem arises how to determine the Young contact angle.[17] This will be discussed in the next paragraph.

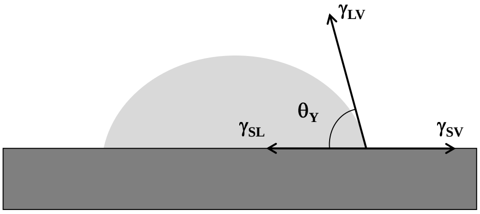

Figure 1. A liquid droplet on an ideal, solid surface.

2.2. Rough and heterogeneous surfaces

2.2.1. Contact angle hysteresis

A real, non-ideal surface is always to some extent rough and/or chemically heterogeneous, and the measured static contact angle turns out not to be unique. There may actually exist a wide range of practically stable apparent static contact angles. The apparent contact angle is defined as the equilibrium contact angle that the liquid makes with the solid surface as observed macroscopically. If liquid is added to a droplet, the apparent contact angle increases until the contact line advances. The contact angle observed when the liquid front is just set in motion is referred to as the advancing contact angle (θ_A). Similarly, if liquid is withdrawn, the contact angle observed when the contact line is just to retract is defined as the receding contact angle (θ_R). The difference between the advancing and receding contact angles is known as contact angle hysteresis, and can sometimes be very large. The hysteresis is generally attributed to chemical heterogeneities and/or roughness. Even in the absence of such imperfections, nearly all surfaces exhibit measurable hysteresis. This inherent hysteresis arises from the interaction between the liquid and solid that was created during spreading. If $\theta_R > 0$, the liquid completely dewets the solid, causing adhesive failure. Alternatively, if $\theta_R \approx 0$ the adhesion between the liquid and the solid is larger than the cohesion of the liquid, leading to drop rupture when the liquid front recedes.[18, 19]

Another way of measuring contact angle hysteresis is to tilt the substrate and set the liquid droplet in motion. The advancing contact angle is measured on the downhill side of the droplet just before the liquid front moves, while the receding contact angle is determined in the similar way, but on the uphill side.[20]

2.2.2. The Wenzel model

For a rough surface, the apparent contact angle may significantly differ from the actual contact angle, located locally on the surface. The actual contact angle, the Young contact angle, is the one needed for the assessment of the surface energy of the solid. In 1936, Wenzel[21] developed the following equation for the relationship between the apparent (θ_A) and the Young contact angle (θ_Y)

$$\cos\theta_A = r\cos\theta_Y \qquad (2)$$

where r is the roughness ratio between the actual and the projected surface area. The Wenzel model is based on the assumption that the liquid completely wets the grooves of the rough surface (Figure 2). The equation thus states that a rough hydrophilic surface ($\theta_Y < 90^o$) should appear more hydrophilic, and a rough hydrophobic surface ($\theta_Y > 90^o$) more hydrophobic than a smooth surface with the same chemical composition.

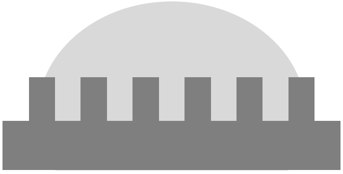

Figure 2. A liquid droplet in the Wenzel state.

2.2.3. The Cassie model

For a chemically heterogeneous surface, the surface energy varies from one location to another, leading to a different value for the Young contact angle at various locations on the surface. In the case of a flat, chemically heterogeneous surface, the wetting is typically described by applying the Cassie equation.[22] For an ideally flat two-component surface the wetting is described by

$$\cos\theta_A = f_1\cos\theta_1 + f_2\cos\theta_2 \qquad (3)$$

where f_1 and f_2 are the area fractions of material 1 and 2, and θ_1 and θ_2 are the Young contact angles on pure materials 1 and 2, respectively. A schematic picture of this case is given in Figure 3. When the chemical heterogeneities are of molecular size, another model has been suggested to better describe the wetting:

$$(1+\cos\theta_A)^2 = f_1(1+\cos\theta_1)^2 + f_2(1+\cos\theta_2)^2 \qquad (4)$$

This expression is known as the Israelachvili equation. [23]

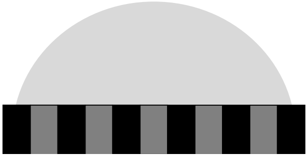

Figure 3. A liquid droplet in the Cassie state.

A rough hydrophilic surface can be considered as a kind of porous material, and the liquid can penetrate the grooves of the surface. A droplet then finds itself on a composite surface of solid and liquid, with a liquid film ahead of the droplet. The top of the textured surface remains dry because of the partial wetting regime (Figure 4). The Cassie equation for this particular case is written

$$\cos\theta_A = f_S \cos\theta_S + 1 - f_S \qquad (5)$$

where f_S is the fraction of solid material and θ_S is the contact angle of pure solid material.[24, 25] This model is later in the thesis referred to as the Bico model. Complete wetting of the substrate is only achieved if the substrate itself becomes wettable (θ = 0).

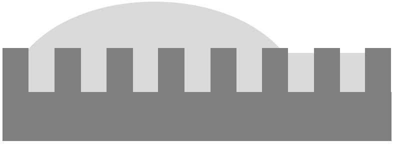

Figure 4. A liquid film is formed ahead of the droplet, when the contact angle is between 0 and a critical value θ_C.

The critical contact angle θ_C, that determines whether the wetting is described by the Wenzel equation (Eq.2) or Eq.5, is given by

$$\cos\theta_C = \frac{1 - f_S}{r - f_S} \qquad (6)$$

If the value of the contact angle lies between 0° and θ_C, the wetting is described by Eq.5, i.e. a liquid film penetrates the texture and the droplet rests on a solid/liquid composite surface. On the other hand, if the value of contact angle lies between θ_C and 90°, the solid remains dry ahead of the droplet, and the wetting is described by the Wenzel equation.[24, 25]

In the case of a rough hydrophobic surface, air bubbles may be trapped in the voids of the rough surface (θ_2 = 180°), and since $f_1 + f_2 = 1$, the Cassie equation can be written as

$$\cos\theta_A = -1 + f_S(\cos\theta_S + 1) \qquad (7)$$

where f_S is the fraction solid material and θ_S is the contact angle of the solid material. This formalism is generally referred to as the Cassie-Baxter equation.[26] In this case, a composite surface of solid/vapor exists below the droplet. This type of wetting is schematically described in Figure 5.

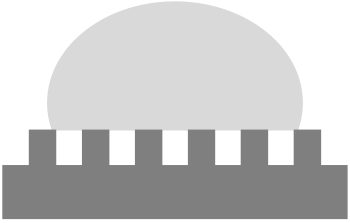

Figure 5. A liquid droplet in the Cassie-Baxter state.

The criterion for air-pockets to form is given by the relation

$$\cos\theta < \frac{f_S - 1}{r - f_S} \tag{8}$$

For a Young contact angle between 90° and a threshold value given by Eq.8, air pockets should be metastable.[24] However, jagged profiles and slope discontinuities increase the possibility of air being trapped, and therefore increase the hydrophobic properties of a surface.[27] The influence of the surface geometry on the entrapment of air was further demonstrated by Hoffman et al.[28] By using rotating glass plates, the transition from complete to partial filling of voids as a function of changing shape of the solid surfaces was demonstrated. The entrapment of air into the grooves of a rough surface is the key when producing superhydrophobic surfaces.

As the Wenzel approach is only valid for homogeneous surfaces, and the Cassie approach is only valid for smooth surfaces, a combination of both equations is needed for a correct description of a rough multi-component surface in the wettable state. For a two-component surface, the roughness of both components of the surface can be accounted for by introducing the parameters r_1 and r_2 describing the respective ratios between the real area of the rough surface divided by the projected two-dimensional areas, and introduce these into the Cassie equation, which then becomes

$$\cos\theta_A = \frac{f_1 r_1}{f_1 r_1 + f_2 r_2}\cos\theta_1 + \frac{f_2 r_2}{f_1 r_1 + f_2 r_2}\cos\theta_2 = F_1\cos\theta_1 + F_2\cos\theta_2 \tag{9}$$

where $F_1 + F_2 = 1$. This formalism is referred to as the Cassie-Wenzel equation in the following.

2.2.4. Transition between Cassie-Baxter and Wenzel states

Several authors have shown that a liquid droplet can be in either a Wenzel or a Cassie-Baxter state on a rough hydrophobic surface, depending on how the droplet is formed. Bico et al.[29] reported that a liquid droplet could be transferred from a Cassie-Baxter state to a Wenzel state when pressed physically. Patankar and co-workers showed that the contact angle of a water droplet that was gently deposited on a rough hydrophobic surface could be modeled with the Cassie-Baxter equation.[30, 31] When the droplet was released from some height on the same surface, the water contact angle was considerably lower. These studies suggest that transitions between two energy states can occur, and that the activation energy of the transition can be fairly low. The geometric parameters of the surface determine the global minimum energy state.[32]

2.2.5. Validity of the Wenzel and Cassie models

Despite the fact that the theoretical values for the contact angles derived from either the Cassie or the Wenzel equations are often in good agreement with experimentally determined contact angles, this is not always the case. For example, Extrand[33] showed that the contact angle measured for a heterogeneous surface cannot be described using the Cassie formalism when the size of the droplet is comparable to the length scale of heterogeneity of the surface, and suggested that the energy balance at the three phase contact line is the decisive parameter. Support for this view was also presented by Gao and McCarthy[34], and they suggested that the Wenzel and Cassie equations are valid only to the extent that the structure of the contact area reflects the ground state energies of contact lines and the transition states between them. The contact line theory was also supported in a very recent theoretical study on chemically heterogeneous surfaces.[35]

Several authors have discussed under what conditions the Cassie and Wenzel models are applicable. McHale[36] emphasized that the original Cassie surface fraction and Wenzel roughness parameter should be viewed as global properties of the surface rather than properties of the contact area below the droplet. Nosonovsky[37] used a surface energy approach to show that the original Wenzel and Cassie equations are only valid for uniformly rough and heterogeneous surfaces. He suggested that generalized Wenzel and Cassie equations should be applied for nonuniformly rough surfaces. Several studies have shown that the Wenzel and Cassie equations are valid only when the scale of the roughness/heterogeneity is small compared to the length of the three phase contact line.[38-40] Marmur[41] emphasized that both the Wenzel and the Cassie equations are approximations, and that their validity increases when the drop size becomes larger with respect to the scale of chemical heterogeneity and roughness.

2.3. Surface free energy determination

A major problem arises when trying to determine the surface free energy of a solid with Young's equation (Eq.1). The solid-liquid interfacial energy γ_{SL} is unknown since it cannot be measured directly. The relationship between γ_{SL} and the solid surface energy γ_{SV} and liquid surface tension γ_{LV} is given by the Girifalco-Good equation[42, 43]

$$\gamma_{SL} = \gamma_{SV} + \gamma_{LV} - 2\phi\sqrt{\gamma_{SV}\gamma_{LV}} \tag{10}$$

where the interaction parameter ϕ is a function of the surface energies. The combining of equation 10 with Young's equation eliminates γ_{SL} giving

$$\gamma_{LV}(1+\cos\theta_Y) = 2\phi\sqrt{\gamma_{SV}\gamma_{LV}} \tag{11}$$

However, the interaction parameter ϕ still remains unknown. Several relationships of ϕ have been suggested. Owens and Wendt[44] used geometric averaging giving

$$\gamma_{LV}(1+\cos\theta_Y) = 2\sqrt{\gamma_{SV}^{d}\gamma_{LV}^{d}} + 2\sqrt{\gamma_{SV}^{p}\gamma_{LV}^{p}} \tag{12}$$

Wu[45] used harmonic mean averaging giving

$$\gamma_{LV}(1+\cos\theta_Y) = 4\frac{(\gamma_{SV}^{d}\gamma_{LV}^{d})}{(\gamma_{SV}^{d}+\gamma_{LV}^{d})} + 4\frac{(\gamma_{SV}^{p}\gamma_{LV}^{p})}{(\gamma_{SV}^{p}+\gamma_{LV}^{p})} \tag{13}$$

Both Eq.12 and Eq.13 splits the surface energy to a dispersion component (d) and a polar component (p) according to

$$\gamma = \gamma^{d} + \gamma^{p} \tag{14}$$

The solution of Eq.12 and Eq.13 requires the contact angle of at least two liquids with known surface tension components. van Oss, Chaudhury, and Good[46] (vOCG) split the surface energy into a Litfshitz-van der Waals component and an acid-base component according to

$$\gamma = \gamma^{LW} + \gamma^{AB} \qquad (15)$$

The LW-component (γ^{LW}) consists of London-, Keesom-, and Debye forces, while the acid-base component consist of Lewis acid (γ^{+}) and Lewis base (γ^{-}) interactions, i.e. hydrogen bonding. These are related to the acid-base component (γ^{AB}) by

$$\gamma^{AB} = 2\sqrt{\gamma^{+}\gamma^{-}} \qquad (16)$$

Eq.11 according to the vOCG model then becomes

$$\gamma_{LV}(1+\cos\theta_{Y}) = 2\sqrt{\gamma_{SV}^{LW}\gamma_{LV}^{LW}} + 2\sqrt{\gamma_{SV}^{+}\gamma_{LV}^{-}} + 2\sqrt{\gamma_{SV}^{-}\gamma_{LV}^{+}} \qquad (17)$$

Eq.17 requires the contact angle of at least three liquids with known surface tension components in order to solve γ_{SV}^{LW}, γ_{SV}^{+}, and γ_{SV}^{-}. van Oss, Chaudhury and Good divided the acid-base contribution of water into two equal (+ and -) contributions (25.5 mN m^{-1}). However, this ratio has appeared to give exaggerated basicity for most solids. Therefore the choice of values of the surface tension components of the probe liquids has been under scientific debate. In order to better reflect the true balance between the acid-base characters of water, a strongly weighed acid contribution has been suggested on experimental and theoretical grounds by a number of authors.[47-50] Much care must also be taken in choosing the proper probe liquids to avoid erroneous results due to mathematical reasons. The difference of the ratios of the basic and acidic parts of the surface tension of the probe liquids should be large in order to obtain reliable results.[51, 52]

3. WETTING OF CHEMICALLY HETEROGENEOUS SURFACES

Micro and nanopatterned surfaces have recently attracted a great deal of interest because of prospects for their wide range of applications, including microelectronics[53], microfluidics[13, 14] and sensing[15] A wide range of different techniques have been used to pattern surfaces, as described in several reviews.[53-55] The wetting properties of patterned surfaces are immensely important in the preparation of microfluidic devices or for the specific targeting of molecules within bioapplications.

One of the most common methods to produce a flat, chemically heterogeneous surface is to use self-assembled monolayers (SAMs) together with some type of soft lithography technique. Patterning of SAMs has for example been carried out by microcontact printing (µCP).[56-58] In µCP an elastomeric stamp (typically PDMS) is wetted with an "ink", and brought into contact with a flat surface, generating a pattern of SAM. This technique was applied to prepare patterned surfaces in a wetting study by Drelich et al.[59] A hydrophobic alkanethiol was assembled on a gold layer with a PDMS stamp, after which a carboxyl-terminated thiol was assembled to create a pattern with well-controlled free energies. Surfaces with alternating parallel hydrophilic (3 µm) and hydrophobic (2.5 µm) stripes and 3 µm × 3µm hydrophilic squares in a hydrophobic field was created in this way. Experimental water contact angles were found to agree with those calculated from the Cassie equation (Eq. 3) when the stripes were tangential to the drop edge for the "parallel stripes" sample or when the drop edge was in the hydrophobic field for the "square" sample. However, when the stripes were normal to the edge for the "parallel stripes" sample or when the drop crossed the "square" pattern sample, the experimentally determined contact angles were much lower than those predicted by the Cassie equation. The authors attributed the divergence to corrugation of the contact line due to contribution of the line tension, and derived a modified Cassie equation that took this effect into consideration. In a later study from the same group on the same type of alternating parallel stripes surface the authors found that the Cassie equation failed to predict the measured contact angle for liquids that have a strong affinity for the hydrophilic stripes.[60] Wetting anisotropy was also found on micropatterned stripes of fluoroalkylsilane monolayers prepared by UV photolithography.[61] The authors suggested that the anisotropy is due to the difference in the energy barrier of wetting between a line and its orthogonal directions, not the line tension or the asperity.

Another commonly applied method to create chemically heterogeneous surfaces is photolithography. Stevens et al.[62] prepared patterned TiO_2 surfaces by irradiating titania wafers with visible light to make them hydrophobic. Subsequently they were irradiated with UV light through photomasks consisting of differently spaced holes (10 µm in diameter) to make the holes hydrophilic. Advancing water contact angles on these surfaces gave good agreement with the Cassie equation. The same group prepared later SiO_2-on-TiO_2 patterns by a combination of standard photolithography and plasma-enhanced chemical vapor deposition.[63] A photoresist was spincoated on a titania wafer and irradiated with UV-light through a photomask. A layer of silica was introduced through plasma-enhanced chemical vapor deposition whereafter the photoresist was removed by thermal lift-off. The resulting surface consisted of SiO_2 patches (10 µm in diameter) in a TiO_2 network. The surface was further hydrophobized with a self-assembled monolayer of fluoroalkylsilane (FAS) and exposed to UV-light. The FAS layer was locally oxidized on the titania, resulting in a patterned surface with a high wettability contrast. Later, the effect of chemical defects on the wetting hysteresis on similar surfaces was investigated.[64] For a hydrophobic surface with high-energy defects, it was observed that the advancing contact angle departed from the Cassie theory, while the receding was in close agreement. Conversely, for low-energy defects in a hydrophilic network, only the receding measurements showed significant departure from theory.

Experimental studies of wetting on chemically heterogeneous surfaces have mainly been restricted to surfaces where the length scale of the heterogeneities is on the micrometer or several hundred nanometers level. This is mainly because of the experimental difficulty in preparing homogeneous patterns on the sub-100 nm length scale. For example, with microcontact printing or standard photolithography it is very challenging to produce patterns of sub-100 nm size. Dip-pen lithography[65] is an alternative method to pattern SAMs on a surface. In this technique, for example alkanethiol molecules are deposited on a gold surface by an AFM tip, which allows patterning down to nanometer size. However, this method is tedious and does not allow patterning of large macroscopic areas. Nanopatterned surfaces have been achieved by self-assembly approaches that were prematurely discontinued in order to yield incomplete surface coverage, thus resulting in patterned surfaces.[66] Wetting studies of nanopatterned surfaces prepared by spontaneous adsorption of octadecylphosphonic acid (OPA) on freshly cleaved mica gave good agreement with Cassie type of wetting.[67] However, such approaches often suffer from inhomogeneous deposition, which can make it difficult to experimentally determine fractional areas with the high accuracy needed for quantitative theoretical analysis. Other methods to fabricate nanopatterned surfaces include the use of colloidal lithography. Titania pillars of 50-90 nm in diameter and 20 nm in height were prepared on silicon wafers by the use of colloidal polystyrene particles as a mask during etching.[15] These materials were further used in biological sensing applications. Recently, the wetting behaviour of nanopatterned surfaces was reported, where nanodots of Au on SiO_x films were prepared by ion-milling.[68] The Au nanodots were further hydrophobically functionalized by immersion into a solution of thiol. This is one of the few wetting studies reported, where nanopatterned surfaces has been studied. The wetting of these materials followed Cassie-Wenzel type of wetting.

In addition to experimental wetting studies on chemically patterned surfaces, several theoretical studies have been performed.[39, 40, 69] They all have in common that a successful modelling with the Cassie equation requires that the size of the heterogeneities should be small compared to the size of the liquid droplet.

4. SUPERHYDROPHOBIC SURFACES

The concept superhydrophobicity has been a known phenomenon since the 1940s, after the novel work of Cassie and Baxter.[26] The interest in this field has expanded greatly during the last decade, much because of the wide range of applications, e.g. self-cleaning surfaces. It is well known that superhydrophobicity (strong water-repellency) is achieved through a combination of low surface energy and roughness. Ever since the superhydrophobic, self-cleaning properties of the Lotus leaf was reported in the late 1990s[3], there have been many attempts to synthetically produce materials with similar water repelling properties, employing methods such as solidification of alkylketene dimers[70], phase separation[71, 72], plasma polymerization[73], photolithography[74], electrochemical deposition[75], and chemical vapor deposition[76] Different methods to prepare superhydrophobic surfaces were recently reviewed.[4]

A prerequisite for a surface to be superhydrophobic is the possibility to trap air within the porous structure. Hence the wetting of superhydrophobic surfaces has been successfully modeled with the Cassie-Baxter equation (Equation 7). In addition to a high static contact angle, a small contact angle hysteresis is essential for a surface to be truly superhydrophobic, as a small hysteresis leads to that a water droplet easily rolls off a surface. This roll-off behavior that Lotus leaves exhibits has been explained by the observed roughness on both micro- and nanometer length scale. This hierarchical roughness has shown to decrease the contact angle hysteresis, by lowering the transition states between metastable states.[77] There have been several attempts to mimic this two-fold roughness.[78, 79] Gao and McCarthy reported a strongly hydrophobic surface with virtually no contact angle hysteresis, which was prepared by treating silicon wafers with methyltrichlorosilane.[80]

In recent years much effort has been made in explaining the mechanisms of superhydrophobic wetting, including contact angle hysteresis and wetting transitions between the Cassie-Baxter and Wenzel states. Many of these studies were recently collected in a review about superhydrophobic wetting.[1]

5. INFLUENCE OF SURFACE ROUGHNESS AND SURFACE FREE ENERGY ON CALCIUM PHOSPHATE PRECIPITATION

The roughness and free energy of the surface are important factors in heterogeneous precipitation of minerals. In many industrial applications, it is important to prevent the formation of mineral scales. For example, in cooling water technology, desalination, paper industry and oil production, scale formation is a serious problem. The surface precipitation (i.e. heterogeneous nucleation) of carbonates, sulfates, phosphates and oxalates of alkaline earth metals is an often encountered problem.[12] On the other hand, rapid nucleation of calcium phosphates may be desired on dental or orthopedic implants in order to enhance their integration to bone tissue, whereas undesirable nucleation occurring in vascular system may result in arteriosclerosis. Thus, control over biomineralization i.e. heterogeneous nucleation of minerals during tissue generation, is essential in modern medicine for developing new biomaterials as well as preventing undesired calcifications. Therefore it is of vital importance to understand the relation between the physicochemical properties of the surface and the heterogeneous nucleation and growth of inorganic deposits.[12, 81-83]

A large number of studies concerning the heterogeneous nucleation and growth of calcium phosphate (CaP) have been reported. Most of the studies have involved calcium phosphate growth on powders. Kinetic studies of nucleation and growth on dispersed particles and macromolecules from a wide range of supersaturated solutions have been performed using the constant composition method.[84-89] Surface precipitation of calcium phosphate on planar surfaces has mainly been studied from solutions with a relatively high degree of supersaturation.[90-94] Heterogeneous nucleation of calcium phosphate is generally believed to be initiated by the adsorption of calcium ions onto negatively charged surface sites.[86, 87, 92, 95] TiO_2 surfaces are good model surfaces for such studies in the sense that the isoelectric point (IEP) of titania is about 6, for both anatase and rutile, which means that the surface carries a net negative charge in aqueous solutions at $pH > 6$.[95] Most CaP precipitation studies reported have been carried out at pH values where the TiO_2 is negatively charged. Furthermore, the solubility of TiO_2 is low, which makes the interpretation of the results more straightforward. A fast nucleation and growth of calcium phosphate on titania has previously been associated with a high Lewis base surface tension component of the substrate.[82, 96] The surface topography at the nanometer level has also been shown to influence the calcium phosphate formation in simulated body fluid. This phenomenon was related to the charge density and the topographical matching of the titania surface and CaP crystal size found in bone.[97-99] Peltola et al. suggested that an average distance (15-50 nm) distribution between surface heterogeneities favored calcium phosphate precipitation.[98]

6. AIM OF THE STUDY

The main aim of the thesis was to study the influence of surface topography and surface chemistry on the wetting properties of TiO_2-based ceramic coatings. In the first part of the study (Papers I-III), pure one component TiO_2 surfaces were studied. The surfaces were prepared using sol-gel dip-coating technology. The aim was to create titania surfaces with various surface topographies by varying the synthesis parameters, e.g. calcination temperature, or with the addition of additives in the sol prior to film preparation. Since the topography might have a large influence on the wettability of a surface, a thorough three-dimensional characterization of the surface is essential. In paper I, the aim was to use standard topographical roughness parameters to describe the topographical characteristics of a series of titania surfaces. Furthermore, the effect of topography on the surface wettability of water was studied. The topographical parameters were calculated from three-dimensional image data captured by atomic force microscopy (AFM). The combined effect of surface topography and surface chemistry of TiO_2 on calcium phosphate precipitation kinetics were investigated in paper II. The aim was to determine which surface topographical characteristics and surface chemical properties that either enhance or slow-down the precipitation kinetics of calcium phosphate.

In paper III the aim was to prepare a superhydrophobic coating by the use of a bioinspired bottom-up approach. The idea was to utilize the spontaneous formation of calcium phosphate on a TiO_2 substrate, followed by hydrophobization through self-assembly.

In the second part of the study (Papers IV-VI), well-ordered nanoperforated layers of TiO_2 on silicon wafers or gold-coated wafers were prepared and characterized. The open pore structure allows selective functionalization of the TiO_2 network and the substrate (SiO_2 or Au) through self-assembly of organic molecules. The aim was to study how the geometrical parameters (pore diameter, wall thickness, layer thickness) and hydrophilic-hydrophobic contrast on the nanometer length scale affects the wetting properties of these materials. The high homogeneity both in terms of the patterning as well as the thickness makes it possible to experimentally determine the important parameters needed for the modeling of the wetting according to existing theories for the wetting of rough and heterogeneous surfaces. Despite the large number of publications on the wetting of rough and heterogeneous surfaces, the number of wetting studies in the literature on surfaces with heterogeneities on the nanometer length scale is quite limited. The nanopatterned surfaces presented in the thesis are ideal model surfaces for wetting studies of nanostructured materials.

7. MATERIALS AND METHODS

7.1. Sol-Gel Synthesis of TiO_2 coatings

Sol-gel technology enables the production of novel nanomaterials with varying morphological and chemical properties. [100] Both organic (metal oxides) and inorganic (salts) can be used as building blocks in the sol-gel process. The precursor is polymerized through hydrolysis and condensation reactions, eventually ending up in the formation of a gel. The final ceramic structure is obtained after drying and/or calcination. Several process parameters (pH, temperature, concentration, aging time) and additives (templates of various kinds and amounts) may be utilized to tune the properties of the end product. In the preparation of sol-gel derived coatings by dip-coating, the substrates are immersed into a dilute sol, and the gel-like coating is formed during substrate withdrawal as a result of solvent evaporation and drying.

7.1.1. Preparation of nonporous and porous TiO_2 coatings

The nonporous titania coatings in papers I-III were prepared by the sol-gel dip-coating technique as described previously[97, 101, 102], but with slight modifications. Briefly, the sol was prepared by mixing tetraisopropyl orthotitanate [$Ti(OCH(CH_3)_2)_4$], ethanol, ethylene glycol monoethyl ether ($C_2H_5OCH_2CH_2OH$), de-ionized water and hydrochloric acid at 0°C with vigorous stirring. The clear sol was kept at 0°C during aging and the dip-coating process. Microscope glass slides (Paper I and II) and commercially pure titanium (Paper II and III) were used as substrate material for the coatings. The dip-coated substrates were calcined at different temperatures and times to obtain morphologically different surfaces. For the preparation of the porous samples, various amounts of polyethylene glycol (PEG) and cetyltrimethylammonium bromide (CTAB) were added to the clear sol which was aged at 40°C prior to dip-coating. During the dipping process PEG, CTAB and the Ti-sol phase separate and a porous structure is formed after calcination of the sample.

7.1.2. Preparation of nanopatterned surfaces with the EISA technique

Mesoporous, thin layers of TiO_2 have been developed using the evaporation induced self-assembly (EISA) technique[103-106], which is related to the surfactant templating technique first reported by the Mobil Oil company in 1992.[107] This technique allows preparation of thin, nanopatterned inorganic films, by using surfactants as templates in the presence of the metal oxide precursor. By varying the size of the template, the diameter of the pores can be tuned.

Thin layers of porous TiO_2 were prepared, by dip-coating the substrate into a solution containing water, ethanol, tetrahydrofuran (THF), the titania precursor ($TiCl_4$), and block copolymers as the structure directing agent. This deposition technique offers the possibility to drastically reduce the layer thickness by increasing the initial solution dilution and by decreasing the quantity of solution to be evaporated. Starting from more and more diluted solutions, one must eventually end up with a homogeneous layer of TiO_2 precursors, bearing a monolayer of periodically dispersed micelles, on the substrate surface. The hybrid monolayer was then heat-treated to eliminate the organic template, which left a network of TiO_2, with the substrate accessible through the nanometer sized craters. A scheme describing the synthesis procedure is given in Figure 6. TiO_2 layers with a thickness between 2 and 15 nm and with pore dimensions ranging from roughly 10 to 35 nm were prepared. Either silicon wafers or gold-coated silicon wafers were used as substrates.

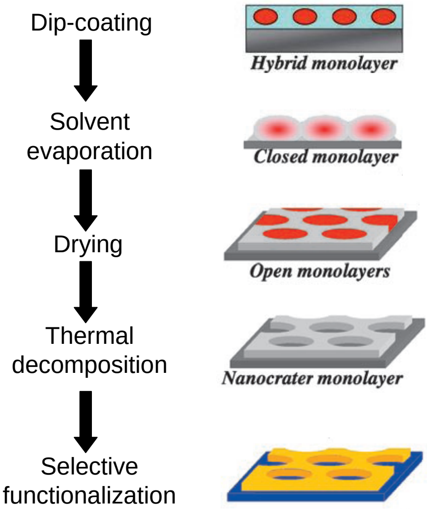

Figure 6. A schematic overview of the formation of nanopatterned layers.

In paper IV and V EO_n-b-$[(E)B]_m$ (poly(ethylene oxide)-block-poly(ethylene-co-butylene) was used as the structure directing agent, while in paper VI a PB-*b*-PEO block copolymer (polybutadiene-*b*-polyethyleneoxide, P2325-BdEO, $MW_{PB} = 32\,000$ g mol^{-1}, $MW_{PEO} = 43\,500$ g mol^{-1}) was used. Nonporous TiO_2 reference films were prepared in a similar way as the porous films but in the absence of the block copolymer. Gold substrates were prepared by vapor deposition on silicon wafers.

7.1.3. Selective functionalization of nanopatterned surfaces

Since the TiO_2 network and the crater bottom (SiO_2 or Au) have different chemistry, these can be selectively functionalized with self-assembled monolayers of various types. In paper IV, the selective functionalization was carried out by attaching two hydrophobic molecules to the TiO_2 and SiO_2 surface, respectively. A perfluorinated function, Zonyl FSE ($F(CF_2)_n(CH_2)_2)_2PO_4NH_4$, n = 3-8, Sigma-Aldrich/Du Pont,) was bound to TiO_2 through the phosphonate group, while vinyl-pentafluorostyrene-diethoxy-silane, VPDS was bound to the SiO_2 surface through the diethoxysilane group. The zonyl functionalization was carried out by immersing the nanopatterned film into an aqueous solution of Zonyl (~0.1 %) for 24 h at room temperature. VPDS grafting was performed by leaving the sample for 24 h in a sealed flask containing a saturated vapor of VPDS. After both grafting steps the samples were washed with water and ethanol. Both grafting processes were completed by a thermal curing at 130°C for 12 h. A schematic picture of the selective functionalization is shown in Figure 7. In paper V, Zonyl FSE was attached to titania while silica or gold was left unfunctionalized. In paper VI, a fluoroalkylsilane, FAS ($CF_3(CF_2)_5(CH_2)_2Si(OC_2H_5)_3$ Sigma-Aldrich) was bound to both TiO_2 and SiO_2, by chemical vapor deposition for roughly 20 hours. The sample was rinsed with water after functionalization. Chemical patterning was induced by irradiation of the sample with UV light ($\lambda = 254$ nm), since the FAS layer oxidizes much faster on titania than on silica. A schematic description of the UV-photopatterning process on the TiO_2@SiO_2 nanopattern is presented in Figure 8.

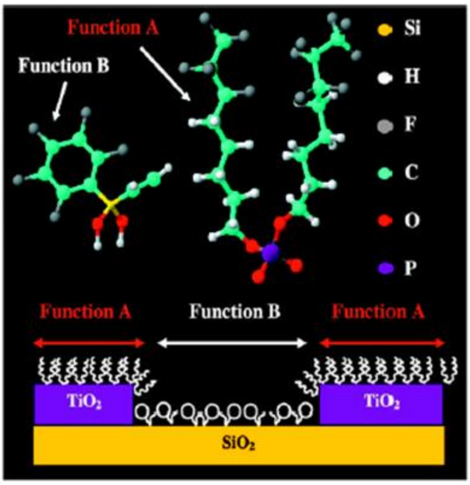

Figure 7. Scheme of the selective funtionalization of a nanoperforated TiO_2 layer on a SiO_2 substrate.

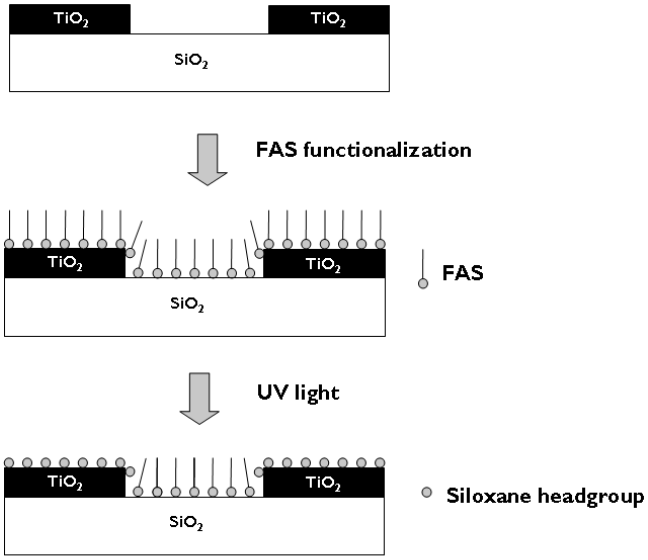

Figure 8. Schematic representation of the photocatalytic decomposition on the $TiO_2@SiO_2$ nanopattern.

7.2. Precipitation of calcium phosphate on sol-gel derived TiO_2 coatings

Supersaturated calcium phosphate solution was prepared by dissolving reagent grade chemicals of NaCl, $CaCl_2{\cdot}2\ H_2O$ (Fluka) and Na_2HPO_4 (Fluka) into distilled, ion exchanged water. The molar concentration of calcium was 3.0 mM, phosphate 1.2 mM and sodium chloride 150 mM. The pH was buffered at 7.4 with tris(hydroxymethyl)aminomethane and 1 M HCl. The solutions were stable for a period of at least 3 weeks. The solution was filtered through 0.22 µm filters before use. The sol-gel prepared titania coatings were cut into pieces having dimensions of $1 \times 1\ cm^2$. The coatings were ultrasonically cleaned in acetone, ethanol and water for 5 + 5 + 5 minutes. The films were then dried in an oven at 40°C for about 4 hours before immersion in 20 ml of supersaturated calcium phosphate solution to give a surface area to solution volume ratio of 0.1. The solutions were kept in polyethylene bottles covered with a tight lid and placed in a shaking water bath at 25°C for a period up to 14 days. At the end of the experiment the coatings were washed with distilled, ion exchanged water and dried at room temperature prior to characterization.

7.2.1. Hydrophobic functionalization of calcium phosphate coatings

In the preparation of the calcium phosphate coatings for the wetting studies in paper III, a higher degree of supersaturation of the calcium phosphate solution was utilized, in order to increase the crystallization rate. The molar concentration of calcium was 3.75 mM, phosphate 1.5 mM (that is 1.5 times the concentration of calcium and phosphate in simulated body fluid (SBF)). The sol-gel prepared titania coatings were irradiated with a low-pressure UV lamp for about 1 hour before immersion in the supersaturated calcium phosphate solution. The solutions were kept in polyethylene bottles covered with a tight lid at 40°C for 5 days, after which an even layer of calcium phosphate had precipitated on the film. At the end of the experiment the coatings were washed with Milli Q water and dried at 40°C. Hydrophobic functionalization of the CaP layer was carried out by immersing the coating in a 0.1 %wt solution of a commercial biodegradable perfluorophosphate surfactant Zonyl FSE (Sigma-Aldrich/Du Pont) in absolute ethanol for 24 hours at room temperature. According to the manufacturer the chemical structure of Zonyl is $(F(CF_2)_n(CH_2)_2)_2PO_4NH_4$, where n = 3-8. The concentration of the perfluorophosphate surfactant was kept low in order to get surfactant attachment only on the CaP surface without formation of intercalated, lamellar structures.

7.3. Surface Characterization Techniques

The most central characterization techniques used in the thesis are described more in detail in this chapter. Additional techniques that will be mentioned in the "Results and discussion" part are X-ray diffraction (XRD), ellipsometry, and cyclic voltammetry.

7.3.1. Contact angle measurements

The most common way of determining contact angles is the sessile drop method. In this technique the profile of a drop suspended on a solid substrate is optically measured with a contact angle goniometer instrument. Modern instruments utilize high resolution cameras and computer analyses to determine the contact angle. Advancing and receding contact angles are generally measured by adding or removing liquid from the droplet with a syringe. Another way of measuring dynamic contact angles is to tilt the substrate and thereby set the droplet in motion.

In this thesis a CAM 200 contact angle goniometer (KSV instruments Ltd., Helsinki, Finland), a Krüss contact angle goniometer, and a DAT 1100 Fibro System were used for determination of contact angles. A liquid droplet was deposited on the solid surface and the static contact angle was determined after a few seconds. Liquid was then added to the droplet and the advancing contact angle was determined just when the liquid front was set in motion. Subsequently, liquid was removed from the droplet and the receding contact angle was determined just when the liquid front was to retract. The contact angles were determined by the software supplied with the instrument.

7.3.2. Atomic force microscopy (AFM)

Atomic force microscopy (AFM) belongs to the family of scanning probe microscopes (SPMs), which cover several related techniques for three-dimensional imaging and probing a surface. The precursor to AFM, Scanning Tunneling Microscope (STM), was invented by Binning et al.[108] in 1982 and allowed imaging of conducting samples down to atomic resolution. In 1986, Binning, Quate and Gerber presented the atomic force microscope, which enabled imaging of insulator surfaces.[109] With its wide range of applications, AFM is nowadays the dominating technique within scanning probe microscopy. The biggest advantage of AFM is that most samples can be investigated in their natural state, which is usually not the case by electron microscopy methods.

In AFM, a probe consisting of an extremely sharp tip connected to a flexible cantilever is scanned over the sample surface using xyz-piezoelectric scanners, which enables very precise and accurate movement. The cantilever is typically silicon or silicon nitride with a tip radius of curvature on the order of nanometers. The interactions between the tip and the surface causes cantilever bending, which is monitored with a laser beam and a photodiode detector. In contact mode AFM, the cantilever deflection is usually kept constant during scanning by a feedback loop between the z-piezo and the photodiode. Hence any change in cantilever deflection due to height differences on the sample surface is compensated by a corresponding change in the z-piezo position. The feedback loop between the piezoelectric scanner and the photodiode thus generates a 3D image of the surface.

In tapping mode AFM[110], the cantilever is driven to oscillate with predetermined amplitude at or close to its resonance frequency by a piezocrystal mounted in the cantilever holder. The tip is then brought closer to the surface until it begins to lightly tap the surface during each oscillating cycle. The amplitude is altered when the tip is approaching the surface due to tip-sample interactions. The relative height position of the cantilever with respect to the sample is therefore adjusted to maintain a constant set-point amplitude during scanning, thus providing the feedback signal for topographical imaging. Tapping mode AFM is more appropriate for imaging soft samples than contact mode AFM, which easily can cause surface damage. Another advantage with tapping mode is the possibility to detect changes in the phase angle of the cantilever probe interacting with the sample. Measured phase-shifts can produce high contrast phase-images, which can give information about material properties, such as stiffness, viscoelasticity, and chemical composition.

The AFM measurements in this thesis were performed in tapping mode in air with a Nanoscope IIIa and V microscope, (Veeco Instruments Inc., Santa Barbara, CA, USA). A SPIP image analysis program[111] were utilized for the image analysis.

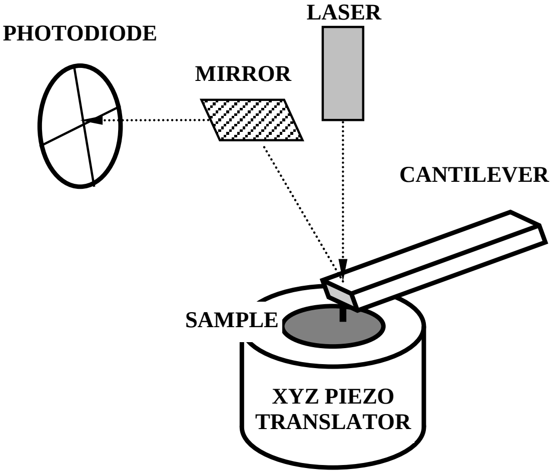

Figure 9. A schematic view of the AFM setup.

7.3.2.1. Topographical roughness parameters

A set of roughness parameters has been developed and standardized for versatile characterization of various surface properties on three dimensions.[112] The parameters are available e.g. in the commercial SPIP image analysis program[111], that has been utilized in this thesis for the characterization of sol-gel derived samples. A list of selected roughness parameters are given in Table 1.

The Root-Mean-Square (RMS) roughness $\mathbf{S_q}$ is the most widely used amplitude roughness parameter that actually gives the standard deviation of height. The two other amplitude parameters in Table 1 tell about the extreme height differences within an image. Obviously, both the peak-peak and ten point height parameters are rather sensitive to noise, i.e. erratic maxima or minima, but the latter is more reliable in this sense because it is calculated as a mean height value of five local maxima and five local minima. For a normally behaving surface the value of $\mathbf{S_z}$ is ca. 10-20 % lower than $\mathbf{S_y}$. A difference larger than this is a clear sign that the values should only be considered as indicative.

Two more useful amplitude distribution parameters are introduced. Surface skewness $\mathbf{S_{sk}}$ describes the asymmetry of the height distribution. A skewness value equal to 0 represents a Gaussian-like surface. Negative values of $\mathbf{S_{sk}}$ refer to a surface-porous sample, i.e. the valleys dominate over the peak regimes. Respectively, the local maxima dominate over the valleys for $\mathbf{S_{sk}} > 0$. Surface kurtosis $\mathbf{S_{ku}}$ gives a measure for the sharpness of the surface height distribution. A Gaussian value for this parameter is 3.0, much smaller values indicate a very broad (heterogeneous) height distribution whereas values much larger than 3.0 refer to a surface with almost quantized height values.

The number of local maxima per unit area is given by the spatial parameter $\mathbf{S_{ds}}$. Besides the number also the form of the local maxima (summits) is of certain interest. Two hybrid parameters have been developed to especially describe the form of the summits: the mean summit curvature, $\mathbf{S_{sc}}$, and the RMS value of the surface slope, $\mathbf{S_{dq}}$.

Most of the above parameters contribute to the effective surface area: the absolute height difference, the number and form of local maxima, among others. A measure for the effective surface area with respect to the projected area is given in percents by the surface area ratio parameter $\mathbf{S_{dr}}$.

Considering the wetting/nonwetting characteristics of a surface, two more parameters should be included. The fluid (or gas) retention indexes indicate the ability of the surface for fluid/gas retention. For a more accurate evaluation the surface is subdivided into two regions in the height scale represented by two different parameters: the core fluid retention index $\mathbf{S_{ci}}$ (the core zone = 20-95% of the total height scale calculated from the absolute minimum) and the valley fluid retention index $\mathbf{S_{vi}}$ (the valley zone = 0-20% of the total height scale calculated from the absolute minimum). The Gaussian values for these parameters are 1.56 and 0.11, respectively.

Table 1. List of selected roughness parameters

Symbol	**Name**	Description
$\mathbf{S_q}$	**RMS roughness**	Standard deviation of the height values
$\mathbf{S_y}$	**Peak-peak height**	Height difference between highest and lowest pixel
$\mathbf{S_z}$	**Ten point height**	Average of five highest local maxima and five deepest local minima
$\mathbf{S_{sk}}$	**Skewness**	Height distribution asymmetry
$\mathbf{S_{ku}}$	**Kurtosis**	Height distribution sharpness (peakedness)
$\mathbf{S_{ds}}$	**Density of summits**	Number of local maxima per unit area
$\mathbf{S_{sc}}$	**Mean summit curvature**	Principal curvature of local maxima
$\mathbf{S_{dq}}$	**RMS slope**	RMS values of the surface slope
$\mathbf{S_{dr}}$	**Developed interfacial area ratio**	Ratio of the increment of the interfacial and projected area
$\mathbf{S_{ci}}$	**Core fluid retention index**	Measure of fluid volume in core zone
$\mathbf{S_{vi}}$	**Valley fluid retention index**	Measure of fluid volume in valley zone

7.3.3. Scanning electron microscopy (SEM)

In electron microscopy an electron beam is used to form magnified images of specimens. The use of electrons instead of light to form images enables a huge improvement in resolution. The resolving power of a modern light microscope is roughly 200 nm, while for a scanning electron microscope it is 1-20 nm, depending on the instrument. The first electron microscopes were developed in the 1930s and 1940s, while the first commercial SEM was introduced in the mid 1960s.[113]

The electrons are usually generated by a tungsten-hairpin gun, and are accelerated through a column towards the sample in the sample chamber. The acceleration is driven by a potential difference (normally 5-20 kV) between the tungsten filament and an anode, called accelerating voltage. Other types of electron sources are Lanthanum-Hexaboride guns and Field-Emission guns, which offers the best resolution.

The beam of electrons is condensed by a condenser lens and focused to a very fine point on the sample by an objective lens. The beam passes through scanning coils located within the objective lens, which deflect the electron beam back and forth in a controlled pattern called a raster. In order for the electrons to hit the sample, both the column and the sample chamber must be kept under vacuum.

The most common imaging mode in SEM is the detection of low-energy secondary electrons. The secondary electrons are ejected from the conduction band of the specimen atoms by inelastic scattering interactions with incident electrons. Since the secondary electrons have such a low energy, only the electrons produced near the surface can escape to the detector. The small sample volume provides and image of high resolution. The electrons are usually detected by an Everhart-Thornley detector, which is a type of scintillator-photomultiplier system. The scintillator converts the secondary electrons into a photon of light, while the photomultiplier produces an amplified electrical signal. This signal is displayed as a two-dimensional intensity distribution, which can be viewed as an image. A large number of secondary electrons are displayed as bright spots, while darker spots are generated by fewer secondary electrons. Small projections on the sample surface appear bright due to the larger area of shorter path length for the escape of secondary electrons than for flat areas. This is the reason behind the three-dimensional appearance in the SEM image.

Another imaging mode in SEM is the detection of backscattered electrons (BSE). Backscattered electrons are beam electrons that have scattered backward. These electrons have a high energy and require a special detector. Backscattered electrons show differences in atomic number within the sample, since heavier nuclei refract more electrons than lighter nuclei. The BSE image is more of a depth image, compared to the secondary electron image which gives better resolution of the surface.

Apart from the required vacuum conditions in SEM, the sample has to be conductive. Insulating samples have to be coated with a conductive layer of carbon, gold or platinum. An advantage with SEM compared to scanning probe microscopy is the possibility to scan large areas of the sample.

The interaction of electrons of high energy with the atoms of the sample also produces X-rays, which are characteristic for the elements present in the sample. The measurement of the energy of these X-rays is generally known as Energy dispersive X-ray spectroscopy (EDS). An EDS unit is often attached to an SEM, therefore the abbreviation SEM-EDS. The detection of the number and energy of the X-rays enables quantitative analysis of the sample. The sampling depth of SEM-EDS is 1-2 µm, making it more of a bulk method compared to the surface sensitive X-ray Photoelectron spectroscopy, XPS. The detection limit of EDS is usually measured in parts per thousand. A FE-SEM (JSM-6335F, JEOL Ltd., Tokyo, Japan) equipped with a Link Inca (Oxford Instruments, Great Britain) EDS unit was used in this thesis. The accelerating voltage during secondary electron imaging and EDS acquisition was 10 kV and 20 kV, respectively.

7.3.4. X-ray Photoelectron spectroscopy (XPS)

X-ray photoelectron spectroscopy (XPS), also known as electron spectroscopy for chemical analysis (ESCA), is a highly surface sensitive technique for chemical characterization of the outermost layer of a sample.[114] The technique was invented in the 1950s, while the first commercial instrument appeared in 1969. In XPS the sample is irradiated with soft x-rays usually generated by either Mg Kα (1253.7 eV) or Al Kα (1486.6 eV) excitation sources under ultra-high vacuum conditions. The photons interact with atoms in the surface region, resulting in emission of photoelectrons whose energies are characteristic of the elements within the sampling volume. The sampling volume extends from the surface to a depth of approximately 5-10 nanometers. The number and kinetic energy of the emitted photoelectrons is detected, which enables quantitative analysis of the sample. The kinetic energy (KE) of the photoelectron is usually converted into binding energy (BE, the energy between the core level and Fermi level) according to

$$BE = h\nu - KE - \phi_S \tag{18}$$

where *hv* is the energy of the incident x-rays and ϕ_S is the work function of the instrument i.e. the energy between the Fermi level and the vacuum level. The binding energy is characteristic of each element but is also influenced by the chemical environment of the atom. XPS is thus a useful tool for obtaining information about chemical states of the elements at the surface of the sample. XPS is applicable to a wide range of materials, also insulating samples. The detection limit for most of the elements is in the parts per thousand range.

The XPS measurements in this thesis were performed with a Physical Electronics Quantum 2000 instrument equipped with a monochromatic Al Kα X-ray source. An operating power of 25 W was used with a spot diameter of 100 µm. An electron flood gun and a low energy ion gun were used for charge compensation. The detector position was at an angle of 45° in relation to the sample surface. The pass energy in the low and high resolution spectral acquisitions was 117.4 and 23.5 eV, respectively. The measured spectra were analyzed with a Multipak 6.1 software.

8. RESULTS AND DISCUSSION

8.1. TiO_2 surfaces with random heterogeneity

8.1.1. 3-dimensional characterization of TiO_2 surfaces by utilizing topographical roughness parameters

TiO_2 surfaces with different morphology and porosity were synthesized by varying the calcination time and the amount of additive. AFM images of four different samples are presented in Figure 10. The image size is 3 µm × 3 µm and the pixel resolution 512 × 512, which results in a sampling interval of 5.86 nm. A smaller image size would not give any additional topographical information in the lateral direction since the radius of curvature of the AFM tips used here was roughly 10 nm. The samples appear to have quite different surface morphology. By utilizing advanced image analysis, the surface properties of the samples can be described by a set of roughness parameters, previously introduced in chapter 7.3.2.1. A selected number of calculated roughness parameters for the samples in Figure 10 are listed in Table 2.

The RMS roughness ($\mathbf{S_q}$) and absolute height ($\mathbf{S_y}$) are increasing from sample A to sample D. The average height parameter $\mathbf{S_z}$ is only slightly smaller than $\mathbf{S_y}$, indicating that the values may be regarded as reliable. Sample A appears to be nonporous, which is also seen in the clearly positive skewness ($\mathbf{S_{sk}}$) value. The very high kurtosis ($\mathbf{S_{ku}}$) value of sample A demonstrates that the peaks have a very narrow height distribution. Also the low valley fluid retention index $\mathbf{S_{vi}}$ and the fairly high number of local maxima per unit area $\mathbf{S_{ds}}$ demonstrates the nonporous character of sample A. Sample B, C and D appear all to be porous. According to the skewness values, however, only sample C shows strong porosity (a clear negative value means that the valleys dominate over the peaks). Sample C also has a large valley fluid retention index $\mathbf{S_{vi}}$ and a small core fluid retention index $\mathbf{S_{ci}}$. Sample B is weakly porous, explained by the slightly negative skewness value and the volume index parameters. It is worth noting that surface porosity does not follow the trend of the RMS roughness. For sample D, despite the large depth of the pores, their small volume is not enough to contribute to the height asymmetry. This conclusion is supported by the volume index parameters $\mathbf{S_{ci}}$ and $\mathbf{S_{vi}}$ which are both close to the Gaussian values. Despite the small pore volume of sample D, the deep pores, with rather long perimeters and, hence, a large wall area, do contribute to the effective surface area.

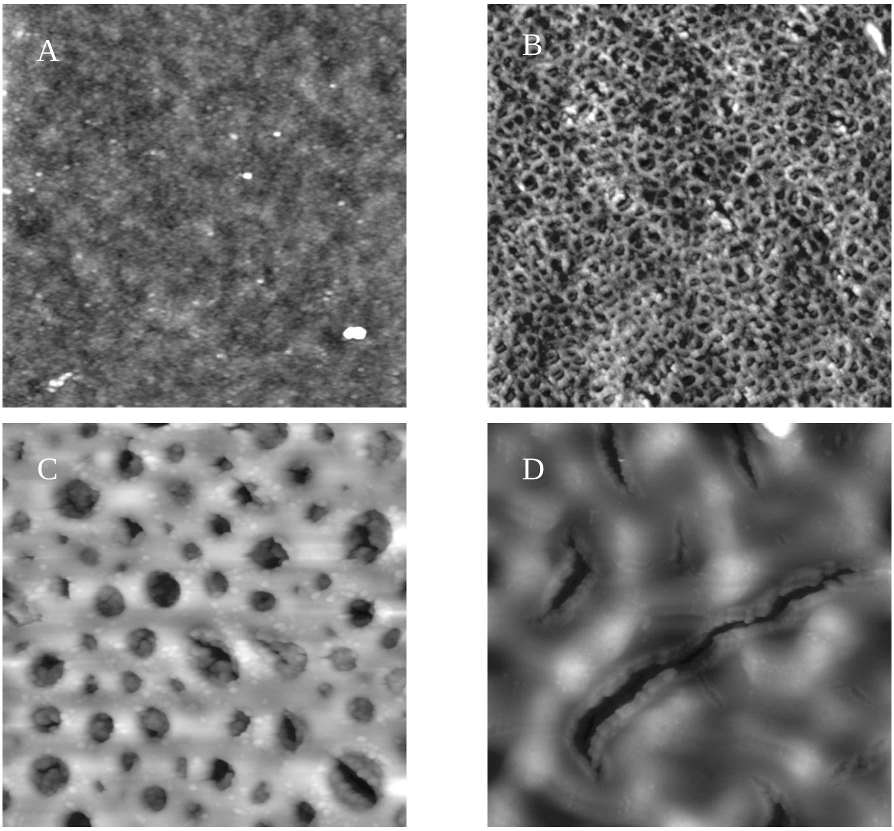

Figure 10. AFM top-view images (3µm×3µm) of different TiO_2 samples. Sample A is prepared without additives. The mass ratios of PEG:CTAB in sample B was 1.25:1.5, sample C 1.25:0.5, and sample D 1.75:0, respectively. Sample A was calcinated at 500°C for 10 min, sample B to D 500°C for 60 min.

The wetting properties of the samples in Figure 8 were studied by measuring static contact angles of water. The values are included in Table 2. According to Wenzel, the relation between the roughness-dependent apparent contact angle θ_A and Young's contact angle θ_Y corresponding to an ideally flat surface is given by

$$\cos\theta_A = r\cos\theta_Y \qquad (2)$$

where *r* is the roughness ratio between the actual and the projected surface area. Since the $\mathbf{S_{dr}}$ parameter gives the increment in surface area related to the projected surface area, it can be utilized to calculate the *r* value in the Wenzel equation according to

$$r = 1 + S_{dr}/100 \tag{19}$$

Table 2. Values of Roughness Parameters and water contact angles for samples of Figure 10.

	Sample A	**Sample B**	**Sample C**	**Sample D**
S_q (nm)	0.5	4.0	18	21
S_y (nm)	12.4	37.7	177	245
S_z (nm)	8.5	32.1	170	230
S_{sk}	3.36	-0.23	-1.29	-0.08
S_{ku}	50.5	3.1	5.9	4.6
S_{ds} (µm^{-2})	815	576	184	343
S_{dr} (%)	0.06	4.9	12.1	7.3
S_{ci}	1.42	1.43	1.09	1.61
S_{vi}	0.092	0.125	0.192	0.123
θ_A (deg)	33	44	43	50
θ_Y (deg)	33	46	50	52

The calculated values of θ_Y are included in Table 2. The correction is largest for the most porous sample and smaller for the other two porous samples. No correction is needed for the smooth, nonporous sample A. The more hydrophilic nature of Sample A compared to the other samples could be explained by the shorter heat treatment at 500° C, possibly resulting in a larger number of remaining OH-groups on the surface. The measured contact angles are still unexpectedly high for a high-energy metal oxide surface as TiO_2. However, high energy surfaces do get contaminated quite fast in a laboratory atmosphere and it appears that cleaning of the surface by sonication in acetone, ethanol and water does not remove all contaminants.[62, 115]

8.1.2. Effect of topography and surface free energy of sol-gel derived TiO_2 coatings on calcium phosphate precipitation

The precipitation of calcium phosphate on sol-gel derived nonporous TiO_2 coatings was studied in Paper II. The properties of the studied surfaces were tuned by heat treatment at a different temperature and length of time. The studied coatings were characterized by AFM and contact angle measurements prior to immersion in supersaturated calcium phosphate solution. Contact angles of three different liquids (water, ethylene glycol, diiodomethane) were determined on the coatings and the surface energy components were calculated according to the van Oss-Chaudhury-Good (vOCG) standard method (Eq.17).[46] In Figure 11 the contact angle of water is plotted against the Lewis base component of the surface free energy and the total surface free energy of the studied coatings. The variation in total surface free energy is quite small, while the differences in the base values are significant. The base component of the surface free energy gives a linear relationship to the water contact angle, which indicates that the interaction with water gives rise to the difference in the base parameter. The base component of the surface free energy has previously been shown to correlate with the kinetics of calcium phosphate formation; a high value of the base parameter leads to faster surface precipitation of calcium phosphate.[82, 96] All of the studied coatings exhibited Lewis acid components of the surface free energy very close to zero. This seems somewhat surprising, since very hydrophilic surfaces should contain a high number of Lewis acidic Ti-OH groups.[116] Furthermore, the low magnitude of the Lewis acid component results in an acid-base (AB) component very close to zero. Therefore it is noted that the values obtained for the base component may be erroneous, due to the inherent sensitivity of the model when the LW-component of the surface free energy is very dominant, as in the present case.

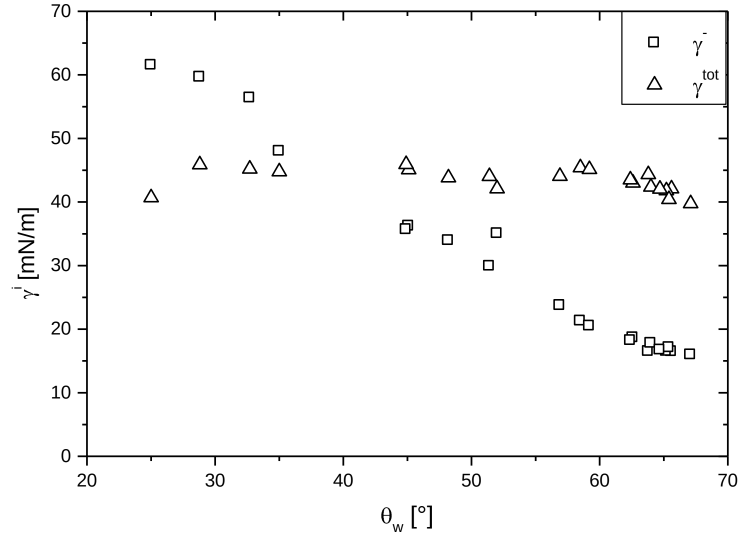

Figure 11. Plot of water contact angle versus total surface energy and Lewis base component of the surface energy for a series of titania coatings.

The combined influence of surface polarity and topography on the precipitation of CaP on a series of TiO_2 coatings is demonstrated in Figure 12. The water contact angle was used in the plot instead of the often used Lewis base component of the surface energy, due to the above discussed reasons. In paper I the influence of topography on CaP formation was studied. The best correlation was found between the precipitated amount and the number of local maxima per unit area (**S$_{ds}$** parameter) on the substrate. A high number (high **S$_{ds}$** value) enhanced CaP formation. Here, the aim was to develop the analysis by considering not only the density (peak-peak distance) but also the amplitude (height) of the local summits. The product of the **S$_{ds}$** and RMS roughness (**S$_q$**) represents the roughness in the plot. It was found that CaP precipitated only on the coatings within the shadowed window during a period of 14 days, evidenced by SEM and XPS. It is worth mentioning that the **S$_q$** parameter alone gave no such correlation. An interesting result is that coatings with a low water contact angle but insufficient roughness precipitated no CaP within two weeks. Respectively, coatings with a high roughness value but fairly high contact angles were equally inactive within this time frame. Also the amount of precipitated CaP increased when moving from the low right hand corner to the upper left hand corner of the window, hence the gradual shading of the window. Additionally, all coatings within the window were mainly of anatase form. No direct correlation between the crystal size and the precipitation was found. The reported $\mathbf{S_q}$ and $\mathbf{S_{ds}}$ values are taken as a mean from 5-10 AFM images. For some coatings the standard deviation of the roughness values was quite large, up to 20 percent. However, the trend is clearly seen from the figure.

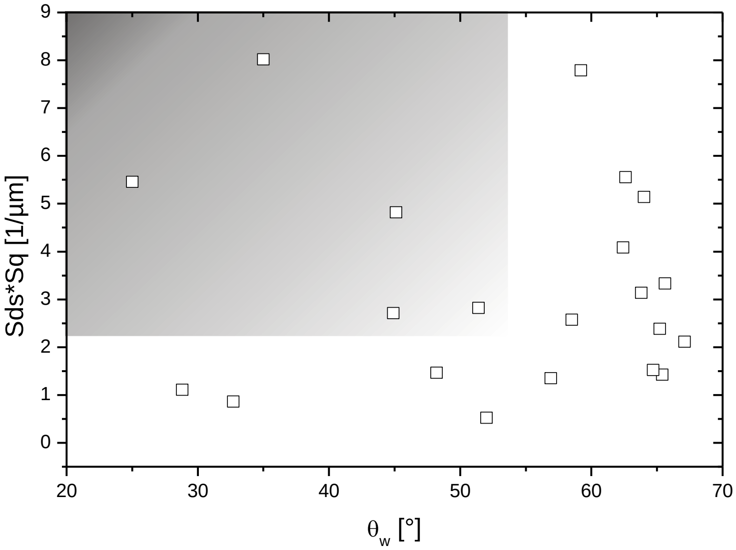

Figure 12. Plot of $\mathbf{S_{ds}}\times\mathbf{S_q}$ roughness parameter as a function of the water contact angle for a series of titania coatings.

Thus, it is suggested that the good correlation observed between CaP precipitation kinetics and the combination of the water contact angle, which is a direct measure of the hydrophilicity of the surface, and surface roughness parameters may be a better explanation for the enhanced surface precipitation kinetics. A more detailed study into the effect of probe liquids and calculation models on the surface energy components of TiO_2 and SiO_2 surfaces is presented in Supporting paper 4.

8.1.3 Wettability studies of hydrophobically functionalized calcium phosphate coatings

An SEM image of a precipitated calcium phosphate (CaP) coating on a TiO_2 substrate is shown in Figure 13. Here, the TiO_2 had been immersed in a supersaturated calcium phosphate solution for 5 days, where the calcium and phosphate concentrations were 1.5 times higher than those used in biological *in vitro* experiments in order to enhance the kinetics of CaP formation. The CaP film is highly porous and consists of platelets aligned at a fairly steep angle relative to the surface. The thickness of the platelets is roughly 200 nm. The CaP layer thickness in this case is about 20 μm, but the CaP film thickness is naturally determined by the time allowed for nucleation and growth of the CaP layer. The observed platelet morphology is comparable to that previously observed for calcium phosphate growth on titania surfaces from solutions with similar compositions and pH.[91, 117, 118] If hydrophobized, such a platelet structure should give rise to a small solid-liquid contact between a water droplet and the material, i.e. a small f_S value in the Cassie-Baxter equation (Eq.7), and thus represent a self-organizing superhydrophobic surface. Furthermore, the superhydrophobicity should be enhanced as a continuous contact line cannot take form on this plate-like structure, which should lead to a small contact angle hysteresis.[73]

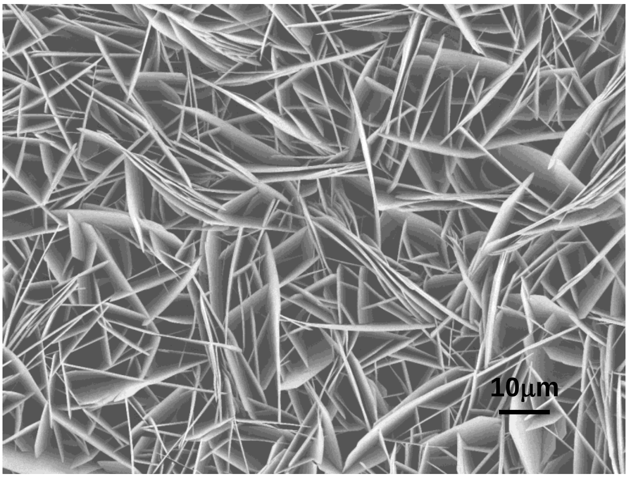

Figure 13. SEM image of a titania coating immersed in supersaturated calcium phosphate solution for 5 days.

Figure 14 shows thin-film X-ray diffraction (XRD) patterns of the precipitated CaP coating. The platelet morphology has previously been observed for octacalcium phosphate (OCP)[117], or a mixture of OCP and hydroxyapatite (HA)[91, 118], which is consistent with the XRD results. The reflection at around 16° (2θ) is characteristic of OCP, while the reflections at 26° and 32° could originate from both OCP and HA. The high intensity of some reflections is due to the plate-like morphology of the precipitated CaP. OCP will typically convert to the more stable HA upon further ageing in solution. Because of the similarities between the structures of OCP and HA epitaxial overgrowths of these phases will easily occur, and the presence of HA cannot be excluded, although the main phase appears to be OCP.[119, 120]

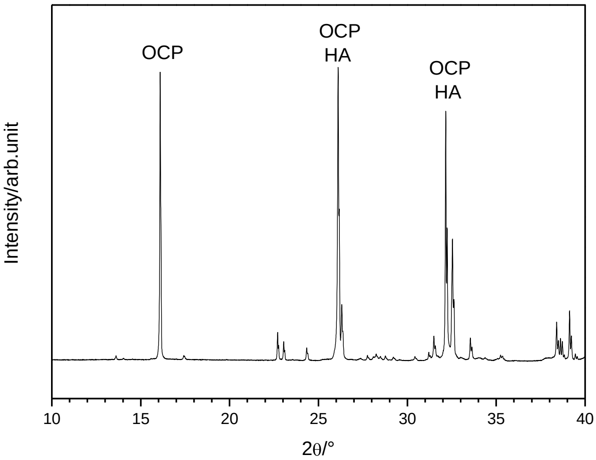

Figure 14. XRD pattern of a titania coating immersed in supersaturated calcium phosphate solution for 5 days. (OCP = octacalcium phosphate, HA = hydroxyapatite)

The successful attachment of zonyl ($(F(CF_2)_n$-$CH_2CH_2O)_2POO^-$, n = 3-8) to the calcium phosphate coating was confirmed by X-ray photoelectron spectroscopy, XPS. The corresponding surface concentrations were 20.06 % C, 33.92% O, 26.99% F, 9.26% P, and 9.77% Ca, the values given in atomic percent. The fitted high-resolution spectra of the carbon C1s signal confirmed the presence of CF_2, CF_3, C-O, and C-C (Figure 15). The observed C=O signal most likely originates from surface contaminants. The area ratio of the CF_2 peak to the CF_3 peak of about 5.5 indicates that the mean number of carbon atoms attached to fluoro-groups in one chain is n = 6.5, which is at the higher end of the range 3-8 given by the manufacturer. This results in a mean fluorine: phosphorus-ratio of 28:1 for one zonyl molecule, which allows us to calculate the portion of phosphorus originating from the zonyl function. By subtracting this contribution from the total amount of phosphorus, a Ca/P ratio of about 1.2 was obtained. The value is close to the Ca/P ratio of 1.3 obtained from SEM-EDS measurements. This ratio is lower than the theoretical value for hydroxyapatite (1.67), but close to the theoretical value of octacalcium phosphate (1.33), again suggesting that OCP is the main calcium phosphate phase. The morphology of the CaP as judged by SEM and XRD remained unchanged upon surface functionalization (results not shown).

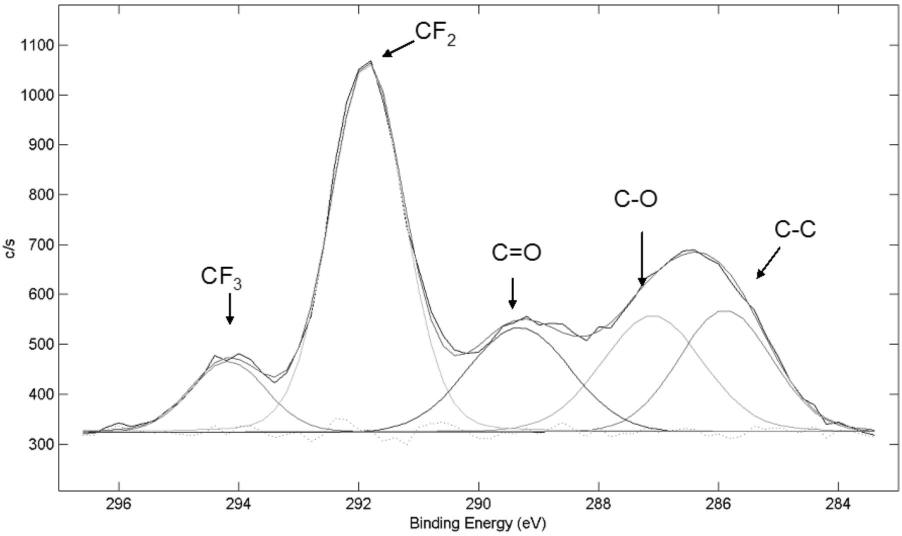

Figure 15. XPS C1s spectra of zonyl-functionalized calcium phosphate.

The wetting properties of the coating are demonstrated by the advancing (>165°) and receding (>150°) water contact angles (Figure 16). No exact value is reported for the contact angle, since it becomes extremely difficult to accurately measure such high contact angles using the sessile drop technique. However, the contact angle values were significantly higher than those previously reported for fluorocarbon-functionalized hydroxyapatite coatings for which advancing water contact angles of 115° or lower have been reported.[121] This difference is mainly attributed to the difference in structural properties between our precipitated calcium phosphate coating and that of coatings prepared by solution deposition of hydroxyapatite particles. The low contact angle hysteresis demonstrates the superhydrophobic properties of the coatings, which was also supported by the observation of free-falling water droplets that bounced and finally rolled off the surface. Non-functionalized CaP surfaces were superhydrophilic, as expected for rough hydrophilic surfaces, and a deposited water droplet fully wetted the coating. The surface functionalization step can also be performed from water, but in that case some re-organization of the CaP film occurred during functionalization, most probably due to dissolution-reprecipitation reactions of the calcium phosphate coating. This leads to a larger contact angle hysteresis than in the case of the coatings functionalized from ethanol, but also in this case the advancing and static contact angles exceeded 160°.

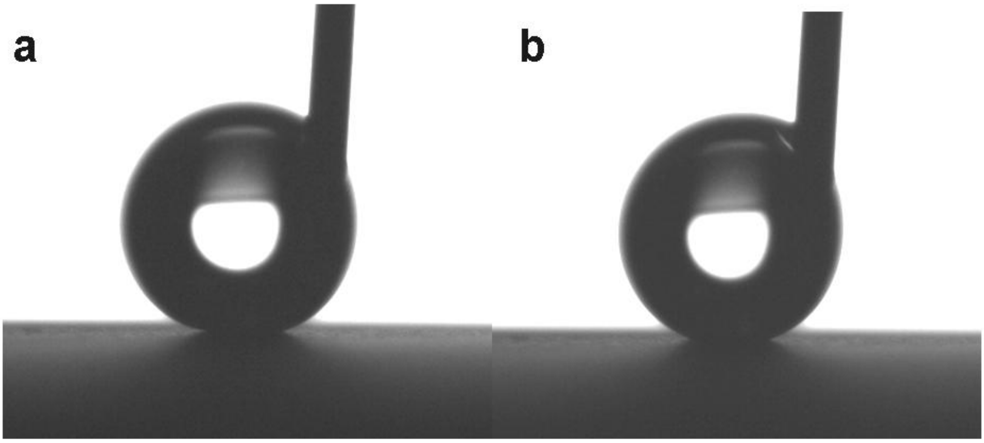

Figure 16. Advancing (a) and receding (b) water droplets on zonyl-functionalized calcium phosphate coatings.

8.2. Nanopatterned TiO_2 surfaces prepared by the EISA technique

8.2.1. Nanopatterned layers with large Wenzel r-values

The nanopatterned surfaces presented in this chapter were prepared using EO_n-b-$[(E)B]_m$ [poly(ethylene oxide)-block-poly(ethylene-co-butylene) as the structure directing agent. The Wenzel *r*-values were in the range 1.7-2 for these films.

8.2.1.1 Determination of f- and r-values

Initially, a detailed structural evaluation of the nanopatterned layers has to performed in order to define all parameters necessary for a correct estimation of the critical parameters needed for evaluation of the contact angle data. In Figure 17 SEM pictures and AFM images of small (mean diameter 11 nm) and large crater (mean diameter 30 nm) TiO_2@Au- and TiO_2@SiO_2 composite surfaces are shown. For the small crater layers one can clearly see a nice ordering of the craters with a narrow crater size distribution and homogeneous crater wall thickness. The crater size distribution is wider for the larger crater layers, but also in this case the layers are homogeneous and of an even thickness. The mean wall thickness was 10 nm for the small crater films, 15 nm for the large crater TiO_2@SiO_2 surfaces, and 18 nm for the large crater TiO_2@Au surfaces. The mean crater sizes and crater size distributions are very similar regardless of whether gold or silica constitutes the substrate. The film thicknesses were also determined by ellipsometry, and were generally in good agreement with those obtained from the AFM measurements. The small crater films had a thickness of 5.5 nm, while the large crater film thickness was 11 nm.

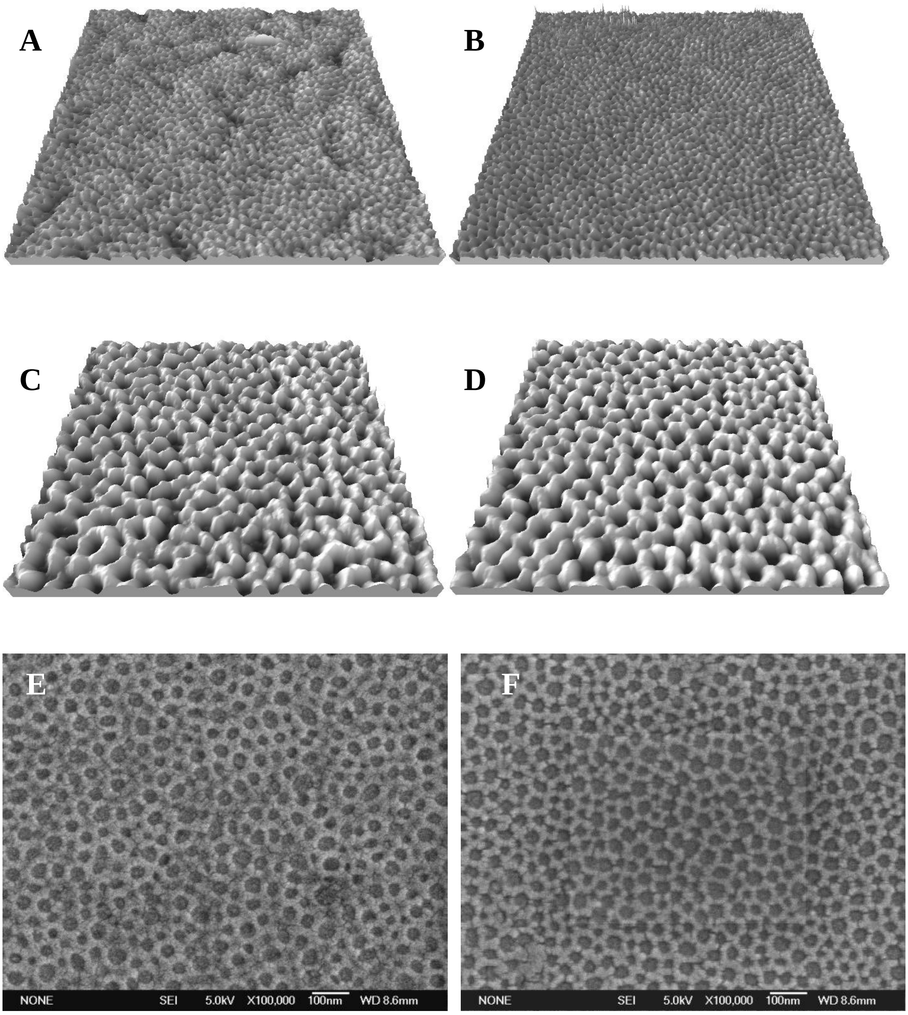

Figure 17. AFM images and SEM micrographs of small and large crater TiO_2 films on gold and silica substrates. A) 1µm*1µm AFM image of small crater TiO_2-film on gold, Z-range 16.4 nm, B) 1µm*1µm AFM image of small crater TiO_2-film on silica, Z-range 13.6 nm, C) 1µm*1µm AFM image of large crater TiO_2-film on gold, Z-range 26.6 nm, D) 1µm*1µm AFM image of large crater TiO_2-film on silica, Z-range 18.8 nm, E) SEM picture of large crater TiO_2-film on gold, F) SEM picture of large crater TiO_2-film on silica.

In order to determine the decisive parameters (*r*- and *f*-values) in the Cassie-Wenzel (Eq.9), Bico (Eq.7) and Cassie-Baxter equations (Eq.5), one unit cell of the nanoperforated layer is approximated as shown in Figure 18.

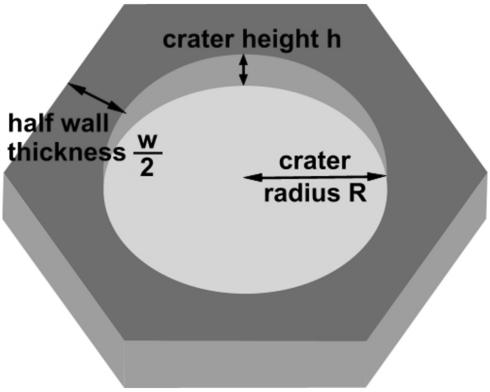

Figure 18. Schematic representation of one unit cell of a nanopatterned film. (R = crater radius, w = wall thickness, h = crater height)

The projected area A_{2D} of the hexagon is given by

$$A_{2D} = 2\sqrt{3}\left(R + \frac{w}{2}\right)^2 \tag{20}$$

Taking the contribution of the crater height *h* (*i.e.* the surface layer thickness)

$$A_{poreheight} = 2\pi \cdot R \cdot h \tag{21}$$

to the overall amount of accessible titania into account, yields the total 3D surface area of the unit cell

$$A_{3D} = 2\sqrt{3}\left(R + \frac{w}{2}\right)^2 + 2\pi \cdot R \cdot h \tag{22}$$

The accessible area of the substrate (Au or SiO_2) of the unit cell is given by

$$A_{substrate} = \pi \cdot R^2 \tag{23}$$

This gives an overall expression for the accessible titania surface $A_{TiO2\text{-}3D}$ of

$$A_{TiO2-3D} = A_{3D} - A_{substrate} = 2\sqrt{3}\left(R + \frac{w}{2}\right)^2 + 2\pi \cdot R \cdot h - \pi \cdot R^2 \tag{24}$$

or, if one takes only the projected area into account

$$A_{TiO2-2D} = 2\sqrt{3}\left(R + \frac{w}{2}\right)^2 - \pi \cdot R^2 \tag{25}$$

The projected area fraction of titania, f_{TiO2}, is then given by

$$f_{TiO2} = \frac{A_{TiO2-2D}}{A_{hex}} \tag{26}$$

Finally, the r-value in the Wenzel equation (Eq.2) is given by

$$r = \frac{A_{TiO2-3D}}{A_{TiO2-2D}} \tag{27}$$

Since the substrate (SiO_2 or Au) is considered to be flat, the Cassie-Wenzel equation (Eq.9) is written as follows:

$$\begin{aligned}\cos\theta_A &= \frac{f_{TiO2} \cdot r}{f_{TiO2} \cdot r + f_2}\cos\theta_{TiO2} + \frac{f_2}{f_{TiO2} \cdot r_1 + f_2}\cos\theta_2 \\ &= F_{TiO2}\cos\theta_{TiO2} + F_2\cos\theta_2\end{aligned} \tag{28}$$

where f_2 is the fraction of SiO_2 or Au. The accessible fraction of the substrate area measured for macroscopic dimensions can also be estimated by cyclic voltammetry curves for the TiO_2@Au films, as the Au substrate is electrically conducting. The calculated *f* and *F* values by both means are presented in Table 3. The larger area of accessible substrate measured by the electrochemical characterization can possibly be explained by the presence of microcracks in the TiO_2 network that were observed by SEM but not taken into account in the fractional area determination based on the AFM and SEM results.

Table 3. Mean crater diameter *D*, wall thickness *w* (both obtained from AFM and SEM images), surface layer thickness *h* (measured with ellipsometry and AFM) and calculated *r*, f_{TiO2} and F_{TiO2} values for the different composite nanoperforated layers.

Sample	**D [nm]**	**w [nm]**	**h [nm]**	**r**[a]	**f_{TiO2} (Cassie-Baxter, Bico)**		**F_{TiO2} (Cassie-Wenzel)**	
					geometric[b]	**cycl.volt.**[c]	**geometric**[d]	**cycl.volt**[d]
TiO_2@Au small craters	11±2	10±2	5.5	1.66	0.75	0.78	0.83	0.85
TiO_2@Au large craters	31±7	18±3	11	1.79	0.65	0.44	0.76	0.58
TiO_2@SiO_2 small craters	11±2	10±1	5.5	1.66	0.75	-	0.83	-
TiO_2@SiO_2 large craters	29±7	15±1	11	1.96	0.63	-	0.76	-

[a] calculated with eq. 27. [b] calculated from AFM and SEM data with eq. 26. [c] determined with cyclic voltammetry. [d] calculated with eq. 28.

8.2.1.2. Wetting studies of unfunctionalized nanopatterns

Water contact angles on unfunctionalized TiO_2@SiO_2 and TiO_2@Au nanopatterns were initially determined. The surfaces were cleaned by heat treatment prior to measurement of the contact angle. Water contact angels on single component TiO_2, SiO_2, and Au surfaces were also determined in order to model the wetting of the composite films according to existing theories for wetting of rough and heterogeneous surfaces. These values are listed in Table 4.

Table 4. Static, advancing, and receding water contact angles on reference surfaces

references	θ_{stat} (deg)	θ_{adv} (deg)	θ_{rec} (deg)
TiO_2	< 5	< 5	0
SiO_2	7 ± 3	10 ± 2	0
Au	80 ± 4	88 ± 1	42 ± 3
Zonyl-TiO_2	88 ± 4	100 ± 1	60 ± 2
Zonyl-SiO_2	25 ± 1	28 ± 1	0
Zonyl-Au	69 ± 2	81 ± 1	37 ± 4

The wetting results on large crater TiO_2@Au and on TiO_2 and Au reference surfaces are presented in Figure 19. Nearly full spreading was observed on the nanopatterned surface, even though the pure Au reference showed a fairly large contact angle. It appears that the continuous network of strongly hydrophilic titania governs the wetting. Theoretical predictions of the wetting were calculated by using *r* and *f* values in Table 3 together with the measured contact angles on the reference surfaces. The Cassie-Wenzel model, represented by the dotted line, clearly overestimates the contact angle. The Bico model (Eq.5) seems however to give good agreement with the experimentally determined contact angle. This model states that the liquid droplet rests on a composite surface of solid and liquid, with a liquid film ahead of the droplet. The wetting results on all unfunctionalized surfaces presented in Table 3 together with theoretical predictions according to the Cassie-Wenzel and Bico models are given in Table 5. The full wetting of the composite surfaces is referred to contact angles <5 degrees.

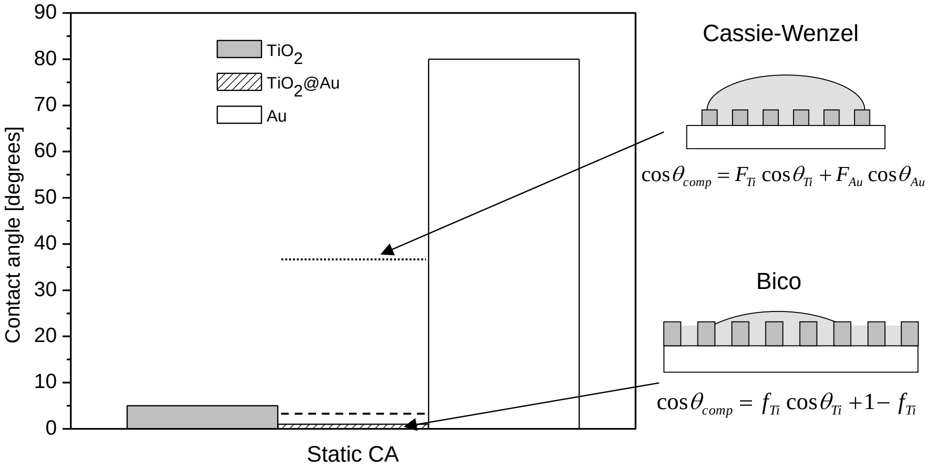

Figure 19. Static water contact angles on TiO_2, Au, and TiO_2@Au nanopattern with large craters. The dotted line and the dashed line represent the theoretical contact angle predicted by the Cassie-Wenzel model and the Bico model, respectively.

Table 5. Experimental water contact angles and theoretical contact angles predicted by the Bico and Cassie-Wenzel models on TiO_2@Au and TiO_2@SiO_2 nanopatterns.

Sample	Contact angle (H_2O)	Bico (deg)						Cassie-Wenzel (deg)					
		geometric			cycl. volt.			geometric			cycl. volt.		
		θ_{stat}	θ_{adv}	θ_{rec}	θ_{stat}	θ_{adv}	θ_{rec}	θ_{stat}	θ_{adv}	θ_{rec}	θ_{stat}	θ_{adv}	θ_{rec}
TiO_2@Au small crater	Full wetting	4	4	0	4	4	0	31	34	17	29	32	16
TiO_2@Au large crater	Full wetting	4	4	0	3	3	0	37	40	20	49	54	27
TiO_2@SiO_2 small crater	Full wetting	4	4	0	-	-	-	5	6	0	-	-	-
TiO_2@SiO_2 large crater	Full wetting	4	4	0	-	-	-	6	7	0	-	-	-

8.2.1.3. Wetting studies of hydrophobic-hydrophilic nanopatterns prepared by selective functionalization of TiO_2

In the next step, a perfluorophosphate surfactant, Zonyl FSE, was selectively attached to the titania portion of the composite films. The selectivity of Zonyl to titania was verified with water contact angle measurements of one-component TiO_2, SiO_2, and Au reference surfaces (see Table 4). Static, advancing, and receding water contact angles on Zonyl-functionalized small crater TiO_2@Au and corresponding references samples are presented in Figure 20. A small droplet (V = 2 µL) was gently deposited on the film, and the advancing and receding contact angles were determined by adding or removing liquid from the droplet. The static and advancing contact angles on the composite surface were higher than any of its constituents, and the wetting could be modeled with high accuracy according to the Cassie-Baxter theory. Thus, despite the very thin film thickness, it is suggested that air is trapped in the craters, resulting in a solid-vapor composite surface. The receding contact angle could not be modeled accurately using the Cassie-Baxter theory. Instead, the Cassie Wenzel theory fitted the experimental results better, though some divergence was still present. This result raises some doubts about whether air was actually located in the craters below the static and advancing water droplets. The Cassie-Baxter state is often referred to as a “slippery” state, in which the hysteresis is small and a droplet easily rolls of a surface. On the contrary, the Wenzel state, in which the hysteresis is large, is called a “sticky” state. However, several authors have stressed the influence of the surface geometry on contact angle hysteresis.[73, 122, 123] For example, on a surface consisting of separated posts, a short discontinuous contact line can take shape, causing less pinning when the contact line is moved. Subsequently, the observed hysteresis is small.[73] Here, on the other hand, a fairly long continuous contact line can take shape on the continuous TiO_2 network, causing pinning when the contact line is moved. Dorrer and Rühe[122] showed that the receding motion of the contact line is a complicated process and that the geometry of the surfaces strongly affects the receding contact angle. Static, advancing, and receding water contact angles of gently deposited small (V = 2μL) droplets on Zonyl-functionalized TiO_2@Au and TiO_2@SiO_2 surfaces are collected in Table 6.

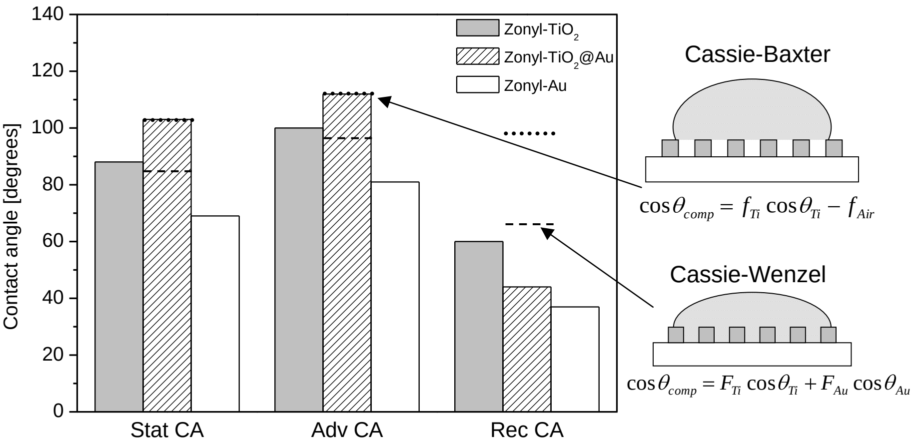

Figure 20. Static, advancing, and receding water contact angles on Zonyl-functionalized small crater TiO_2@Au nanopattern with small craters and Zonyl-treated TiO_2- and Au reference surfaces. The droplet size for the static contact angles was 2 µL. The dotted lines represent the theoretical contact angles predicted by the Cassie-Baxter model, the dashed lines represent the theoretical contact angles predicted by the Cassie-Wenzel model.

Table 6. Static, advancing, and receding water contact angles on Zonyl-functionalized nanopatterns together with predicted contact angles according the Cassie-Baxter and Cassie-Wenzel models.

Sample	Contact angle H_2O (deg)			Cassie-Baxter (deg)						Cassie-Wenzel (deg)					
				geometric			cycl. volt.			geometric			cycl. volt.		
	θ_{stat}	θ_{adv}	θ_{rec}	θ_{stat}	θ_{adv}	θ_{rec}	θ_{stat}	θ_{adv}	θ_{rec}	θ_{stat}	θ_{adv}	θ_{rec}	θ_{stat}	θ_{adv}	θ_{rec}
Zonyl-TiO_2@Au small crater	103	112	44	103	112	83	101	111	80	85	97	57	85	97	57
Zonyl-TiO_2@Au large crater	119	127	23	109	118	91	123	130	110	84	95	55	80	92	51
Zonyl-TiO_2@SiO_2 small crater	107	116	47	103	112	83	-	-	-	79	90	54	-	-	-
Zonyl-TiO_2@SiO_2 large crater	121	128	13	110	119	93	-	-	-	76	85	52	-	-	-

To further investigate the wetting characteristics of the nanopatterned surfaces, larger droplets (~6.5 µL) were released from some height onto the Zonyl-functionalized nanopatterned layers. The static contact angles measured for both small and large crater nanoperforated layers were significantly lower (<90°) than for the gently deposited small droplets. As an example, snapshots measured for small crater Zonyl-TiO_2@Au surfaces are shown in Figure 21. It thus seems to be a transition from a Cassie-Baxter state to a Cassie-Wenzel state, suggesting that the craters become filled with liquid when a larger droplet is free-falling onto the surface. Similar tests were also done on smooth TiO_2 and Au-reference surfaces, and no difference in contact angle compared to the gently deposited droplets was observed. For these larger droplets, the static contact angles of the zonyl-functionalized composites are better described by the Cassie-Wenzel theory, suggesting that the energy barrier between the Cassie-Baxter and the Cassie-Wenzel states is low. This activation energy can be overcome by letting a larger droplet fall from some height onto the surface, which is in agreement with both experimental observations[30, 31] and theoretical predictions.[124] Very interestingly though, if more liquid was added to this large droplet, the advancing contact angle increased to similar values as for the small droplets. The situation is illustrated in Figure 22 for small crater TiO_2@Au. This result, together with the receding contact angle data, gives some indication that the craters could be filled with liquid below the droplet, and that the three-phase contact line is the decisive factor determining the contact angle.[33, 34] The good agreement between the experimentally determined contact angle values and those derived based on either the Cassie or the Wenzel equations would in that case be related to the fact that the area fractions describe the surface composition along the three phase contact line well for these nanopatterned films.

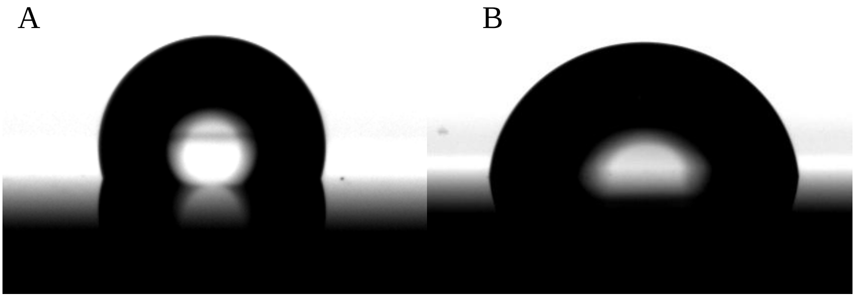

Figure 21. Water droplets on Zonyl-TiO_2/Au films with small craters a) small water droplet (Drop volume ≈ 2 µL, θ_{stat} = 103°) gently deposited and b) large droplet dropped from some height (Drop volume ≈ 6,5 µL, θ_{stat} = 85°).

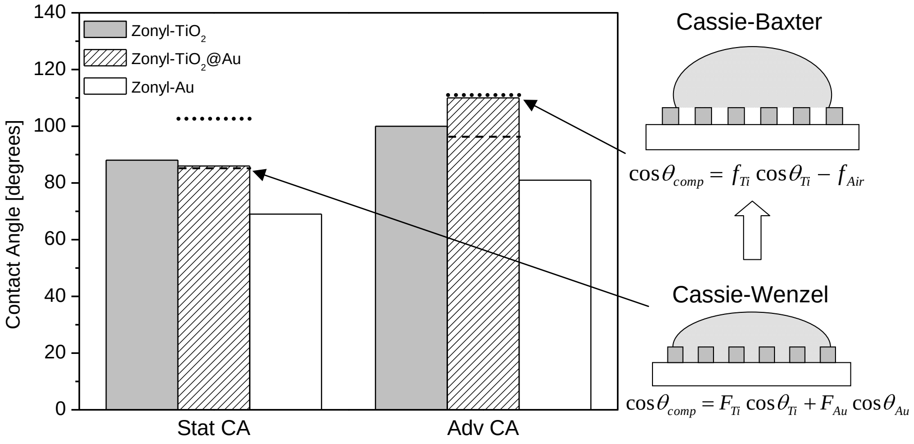

Figure 22. Static and advancing water contact angles on Zonyl-functionalized small crater TiO_2@Au nanopattern and Zonyl-treated TiO_2- and Au reference surfaces. The droplet size for the static contact angles was 6.5 µL and the droplet was free-falling on to the surface. The dotted lines represent the theoretical contact angles predicted by the Cassie-Baxter model, the dashed lines represent the theoretical contact angles predicted by the Cassie-Wenzel model.

8.2.2. Nanopatterned layers with small Wenzel r-values

For the preparation of the TiO_2@SiO_2 nanopatterns presented in this chapter a PB-*b*-PEO block copolymer (polybutadiene-*b*-polyethyleneoxide) was used as the structure directing agent. The Wenzel *r*-values of these films were close to 1.

8.2.2.1.Wetting studies of hydrophilic-hydrophobic TiO_2@SiO_2 nanopatterns prepared by UV-photopatterning

AFM images of a thin nanopatterned TiO_2@SiO_2 composite surface is presented in Figure 23. The images show hexagonally ordered craters of silica in a network of titania. The mean crater diameter and wall thickness is roughly 30 nm as determined from image analysis. The estimated film thickness obtained from AFM cross section analysis is approximately 2 nm. These structural dimensions give rise to a fraction of titania of roughly 80% in the composite film, by approximating one unit cell as described in chapter 8.2.1.1. Furthermore, these dimensions give rise to a roughness-value according to Wenzel of 1.08, to compare with *r*-values of 1.7-2.0 for the thicker nanopattern films presented in chapter 8.2.1. An *r*-value close to 1 suggests that the influence of roughness on the wetting should be small for this type of nanopatterned surface.

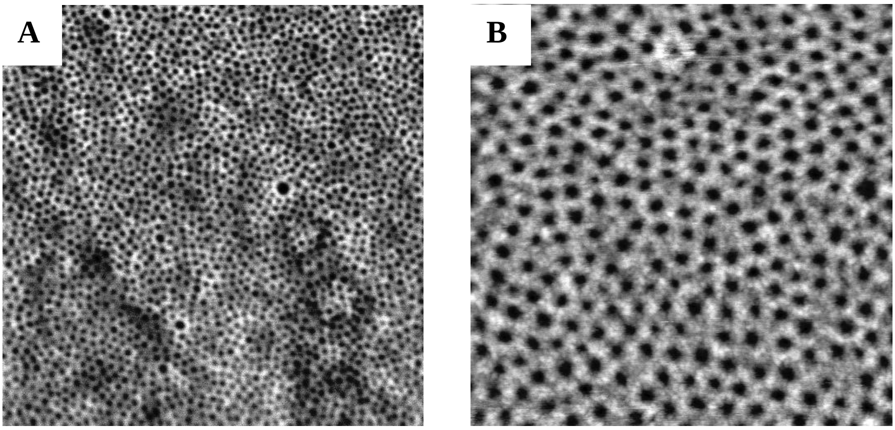

Figure 23. 3 µm× 3 µm (A) and 1 µm×1 µm (B) AFM images of a $TiO_2@SiO_2$ nanopatterned surface. The Z-range in the images is 1.93 and 3.40 nm, respectively.

The nanopatterned $TiO_2@SiO_2$ film was hydrophobized by the formation of self-assembled monolayers of a fluoroalkylsilane (FAS), as described in chapter 7.1.3. The successful attachment was verified with XPS. Furthermore, the decomposition of FAS as a function of UV irradiation time was studied with XPS. XPS spectra of the F 1s signal are presented in Figure 24. As expected, the intensity of the F peak decreases as a function of UV exposure. The area fraction of covered FAS, f_{FAS}, was then calculated from the F/Ti ratio, normalized against the F/Ti ratio before UV treatment and by assuming full initial coverage of FAS. XPS derived F/Ti ratios and f_{FAS}-values as a function of UV exposure are listed in Table 7. The calculation of f_{FAS}-values from F/Si ratios resulted in the same *f*-values within the experimental error, showing that any influences of the differences in X-ray sampling volume induced by the presence or absence of FAS on the *f*-values can be neglected.

Table 7. XPS derived F/Ti ratios and calculated f_{FAS}-values as a function of UV irradiation time for FAS-functionalized $TiO_2@SiO_2$ nanopatterns.

UV time [min]	**0**	**5**	**15**	**30**	**60**	**120**
F/Ti	2.34	2.03	0.91	0.72	0.42	0.32
f_{FAS}	1	0.87	0.39	0.31	0.18	0.14

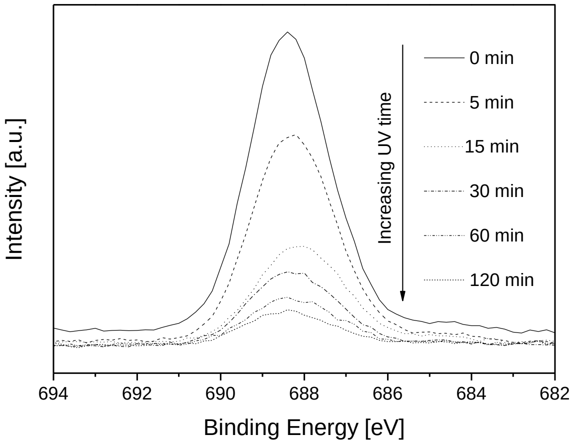

Figure 24. XPS spectra of the F 1s signal on FAS-functionalized $TiO_2@SiO_2$ nanopatterns as a function of UV irradiation time.

The decomposition of FAS as a function of UV treatment time was also studied by water contact angle (CA) measurements on FAS-functionalized composite, titania-, and silica reference samples. Results on static water contact angles are presented in Figure 25. Before UV treatment, all FAS-functionalized surfaces were hydrophobic with static water contact angles of 109˚ (FAS-TiO_2), 106˚ (FAS-SiO_2), and 108˚ (FAS-$TiO_2@SiO_2$). These contact angle values are very close to values typically observed on fully fluorinated surfaces, which indicates that full coverage of the fluoroalkylsilane layer on all surfaces is attained.[63] The close agreement between the contact angles suggests that the surface roughness of the $TiO_2@SiO_2$ composite has a negligible effect on the wetting. The water contact angle on a FAS-functionalized SiO_2 reference remained unchanged even after several hours of UV treatment, which shows that the FAS layer is perfectly stable on a pure silica surface. On the other hand, the water contact angle on the FAS-functionalized TiO_2 reference sample decreased to below 5 degrees after only 5 minutes of UV treatment. The very different behavior of silica and titania is due to the large difference in photocatalytic activity of the two oxides.[63, 125, 126] For the FAS-coated $TiO_2@SiO_2$ composite sample, the water contact angle decreased gradually as a function of UV treatment time. If assuming a TiO_2 portion of 80%, as estimated from the AFM image analysis, one would expect a water contact angle of roughly 40° (according to Eq.3) on the composite surface when the FAS layer has oxidized from the TiO_2 part. After 2 hours of UV irradiation, a static water contact angle of 32° was measured on the composite surface, which could be an indication of that the FAS layer has started to oxidize also from the silica part of the composite film. The water contact angle continued indeed to decrease at longer than 2 hours of UV irradiation (results not shown here). In a previous study on the decomposition of octadecyltrichlorosilane (OTS) on micrometer sized $TiO_2@SiO_2$ patterns, the authors suggested that at prolonged UV irradiation oxidizing species photogenerated on the TiO_2 surface reach and attack OTS chains on the SiO_2 domains.[126] This effect could possibly be magnified when the SiO_2 domains are of nanometer size, even though a fluoroalkylsilane (FAS) should be much more stable than an alkylsiloxane against UV irradiation.

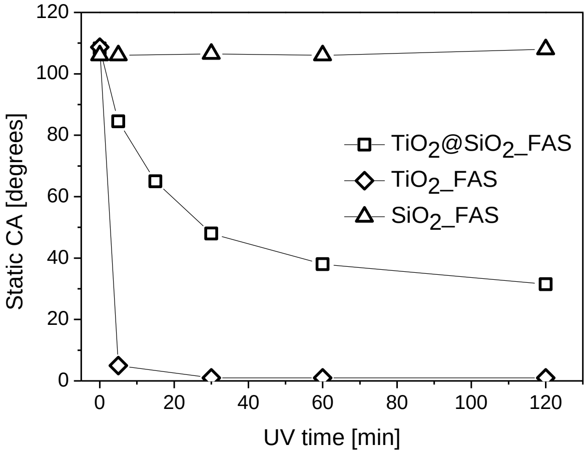

Figure 25. Static water contact angles (CA) as a function of UV irradiation time on FAS-functionalized $TiO_2@SiO_2$ composite-, TiO_2, and SiO_2 surfaces.

Advancing CA, receding CA, and CA hysteresis on the FAS treated $TiO_2@SiO_2$ composite as a function of UV irradiation time is presented in Figure 26. Before UV treatment, the degree of hysteresis on the FAS-functionalized TiO_2- and SiO_2 references was very similar to the composite, again indicating that the roughness of the nanopatterned layer has a minimal influence on the wetting. The low hysteresis prior to UV irradiation also indicates full coverage of the FAS layer. The CA hysteresis increases initially with longer UV irradiation time and reaches a maximum value at around 40° between approximately 30 min and 1 h of UV irradiation, whereafter a small decrease could be observed. While there are a large number of publications on the hysteresis behavior on rough, hydrophobic surfaces (see[73, 122, 127]and references therein), the number of similar studies on flat, chemically heterogeneous surfaces is more limited. Most of the work has been restricted to materials with heterogeneities on the micrometer length scale, mainly because of the experimental difficulty in preparing homogeneous patterns of sub-100 nm length scale.[59, 60, 64] In a theoretical study on the hysteresis behavior on alternatively aligned horizontal apolar ($\theta = 70^\circ$) and polar stripes ($\theta = 0^\circ$), Fang et al.[128] suggested that the hysteresis vanishes at a critical stripe width between 6 and 12 nm. The authors also suggested that the contact angle hysteresis attains its maximum value at a fraction of apolar material of roughly 0.5 at a stripe width of 37.8 nm, and both increasing and decreasing *f*-values reduces the hysteresis. A shift of the maximum hysteresis value towards lower fraction of apolar material was observed for increasing stripe width. The hysteresis behavior of the FAS-functionalized $TiO_2@SiO_2$ nanopattern as a function of UV irradiation time appears to follow a similar pattern as in reference 128. The degree of hysteresis is also dependent on the difference in surface energy between the heterogeneities. Here, the maximum wettability contrast between the FAS-layer and the oxidized titania part is most probably magnifying the hysteresis.

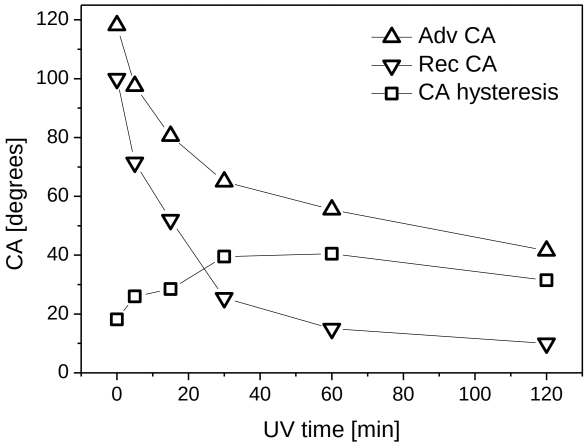

Figure 26. Advancing (up-triangles) and receding (down-triangles) water contact angels together with the contact angle hysteresis (squares) on the FAS-functionalized $TiO_2@SiO_2$ composite as a function of UV irradiation time. (CA = contact angle)

In order to study the decomposition of FAS, existing theories for the wetting of chemically heterogeneous surfaces were applied. The area fraction covered with FAS, f_{FAS}, on the $TiO_2@SiO_2$ composite after a certain time of UV exposure, was calculated according to the theories of Cassie (Eq.3) and Israelachvili (Eq.4), by inserting measured water contact angles on the composite and corresponding reference samples into the equations. The f_{FAS}-value according to Cassie is given by

$$f_{FAS} = \frac{\cos\theta_{COMP} - \cos\theta_{TiO2}}{\cos\theta_{FAS} - \cos\theta_{TiO2}} \tag{29}$$

and according to Israelachvili by

$$f_{FAS} = \frac{(1-\cos\theta_{COMP})^2 - (1-\cos\theta_{TiO2})^2}{(1-\cos\theta_{FAS})^2 - (1-\cos\theta_{TiO2})^2} \tag{30}$$

where θ_{COMP} is the water contact angle on the composite surface, θ_{TiO2} is the contact angle on the UV treated TiO_2 reference surface, and θ_{FAS} is the contact angle on the hydrophobic FAS layer. The result of such calculations is presented in Figure 27 and 28. Fractions of remaining FAS were calculated from static, advancing and receding water contact angles according to both theoretical models. The static contact angles used in the calculations are presented in Figure 25, while advancing and receding contact angles on the composite surface are given in Figure 26. 112° and 100° were used as advancing and receding contact angles for the hydrophobic FAS-layer, while 5° and 0° was used for the UV treated TiO_2 reference surface. Due to contact angle hysteresis, advancing and receding contact angles give rise to different f_{FAS}-values. The Cassie model (Figure 27) generates slightly smaller f_{FAS}-values than the Israelachvili (Figure 28) model. Furthermore, to test the validity of the wetting models on the TiO_2@SiO_2 nanopattern, f_{FAS}-values calculated from the contact angle data were compared with f_{FAS}-values determined with XPS. The area fraction of FAS according to XPS measurements gave generally a good agreement with f_{FAS}-values determined from the static contact angles, with a slightly better fit to the Cassie theory compared to the Israelachvili theory, at least at longer times of UV exposure. This is quite expected since the Israelachvili model was derived for chemical heterogeneities of atomic or molecular dimensions. The Israelachvili theory also produces a larger difference between the f_{FAS}-values derived from advancing and receding contact angle data. The good fit of the f-values derived from the Cassie and Israelachvili models to the XPS results suggests that these models are valid to describe the wetting on our nanopatterned surfaces, where the length scale of the heterogeneities is very small compared to the size of the droplet. Several studies have shown that the Cassie equation is valid only when the scale of the heterogeneity is small compared to the length of the three phase contact line.[38-40] It has also been emphasized that the Cassie equation is an approximation that improves when the drop size becomes larger with respect to the scale of chemical heterogeneity.[41]

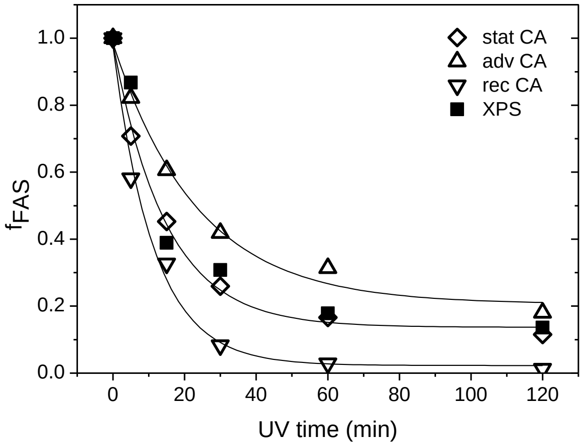

Figure 27. f_{FAS}-values calculated from static (diamonds), advancing (up-triangles) and receding (down-triangles) contact angles according to Cassie's model together with XPS derived f_{FAS}-values (filled squares) on FAS-functionalized TiO_2@SiO_2 nanopatterns as a function of UV irradiation time. The solid lines fitted to the contact angle derived f_{FAS}-values are included as guidance for the eye.

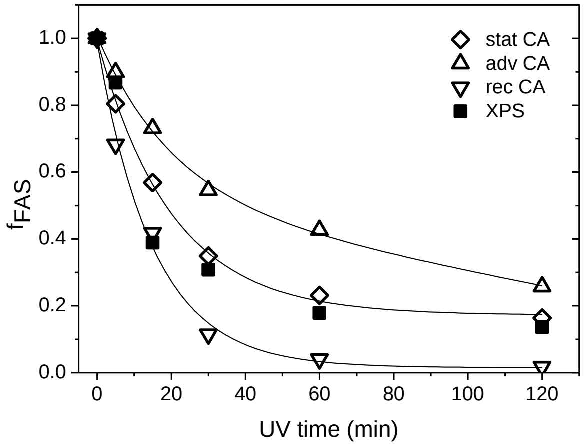

Figure 28. f_{FAS}-values calculated from static (diamonds), advancing (up-triangles) and receding (down-triangles) contact angles according to Israelachvili's model together with XPS derived f_{FAS}-values (filled squares) on FAS-functionalized $TiO_2@SiO_2$ nanopatterns as a function of UV irradiation time. The solid lines fitted to the contact angle derived f_{FAS}-values are included as guidance for the eye.

Since the fraction of FAS calculated from static water contact angles in most cases gave the best agreement with XPS derived f_{FAS}-values, it is suggested that the static CA is a good approximation of the most stable contact angle. Modeling of the wetting according to advancing CA data and receding CA data deviates from the XPS derived f_{FAS}-values, apart from a few exceptions. Assymetric wetting hysteresis has previously been reported on chemical defects of micrometer size.[64] It was found that the Cassie equation gave a good fit to measured receding water contact angles for high-energy defects in a low-energy network, while the advancing contact angle departed from theory. Conversely, the advancing contact angle gave good agreement with Cassie's theory for hydrophobic defects in a hydrophilic network, while the receding measurements deviated. However, the advancing contact angle reported in these studies was a static advancing contact angle, defined as the contact angle when the movement of the liquid front ceases. The static contact angles reported here are comparable to the static advancing contact angles reported in reference 64. In another recent work, the effect of length scale on the hysteresis behavior on chemically heterogeneous surfaces was studied by the use of a phase field theory.[129] It was concluded that the Cassie theory is applicable for both advancing and receding contact angles only in the limit of vanishing length scale. For heterogeneities of micrometer length scale, both advancing and receding CAs deviated from Cassie behavior. The deviation was found to be asymmetric and depended on the energy of the defect with respect to the continuous phase. However, the wetting contrast between the component materials in ref. 129 was very different ($\theta_A = 145^\circ$ and $\theta_A = 95^\circ$) than for the UV-photopatterned $TiO_2@SiO_2$ surface. The large wetting contrast between the oxidized titania part ($\theta_{stat} \approx 0°$) and the FAS-layer ($\theta_{stat} = 108°$) probably affects the degree of hysteresis, even though the length scale of heterogeneity is small. The use of static CA in the Cassie equation seems therefore to give a better estimation of the remaining fraction of FAS, as these *f*-values give a good agreement with fractions determined by XPS.

9. CONCLUSIONS AND OUTLOOK

The effect of surface roughness and surface chemistry on the wetting properties of sol-gel derived TiO_2-based ceramic coatings has been studied. The topography of one-component TiO_2 coatings with random heterogeneities was described with a set of roughness parameters, obtained from image analysis of AFM micrographs. It was shown that the most commonly used parameter, the RMS roughness, is not specific enough to describe the complex relation between various surface features and phenomena such as wetting and precipitation. The combined effect of topography and surface wettability on the precipitation kinetics of calcium phosphate (CaP) on the coatings was further investigated. It was found that a hydrophilic coating together with a high roughness value is more favorable to initiate the formation of CaP. The roughness was represented by the product of the RMS roughness and the number of local maxima per unit area.

The preparation of a superhydrophobic coating by utilizing a simple bioinspired bottom-up approach was further demonstrated. The coating is self-organizing by the spontaneous formation of CaP on sol-gel derived TiO_2 coatings. The CaP coating was hydrophobized by self-assembly of a perfluorophosphate surfactant. The coating exhibited extreme water-repellency, as a result of the topography of the low-energy surface. The CaP coating consisted of platelets aligned at a fairly steep angle relative to the surface, which resulted in a minimized solid-liquid contact between a deposited water droplet and the hydrophobized surface. The described methodology could also be extended to calcium carbonate surfaces, thus widening the applicability to industrially relevant surfaces. For example, the methodology could be used to modify calcium derived scales at an early stage of scale formation, thus preventing further scale formation.

In the second part of the thesis, the wettability of well-ordered nanopatterns of TiO_2 on silica and Au substrates was studied. Nanopatterned films were produced by evaporation-induced self-assembly (EISA) using dip-coating. EISA involves nanopatterning via the liquid deposition of condensable inorganic precursors in the presence of surfactant micelles. Dilute precursor solutions were used so that only a monolayer of micelles were deposited, and a nanopatterned surface was obtained upon drying-induced collapse of the micelles. The organic template was finally removed by calcination. The crater dimension can be tuned between roughly 10 and 50 nm depending on the molecular weight of the surfactant used as the template. This approach can easily be scaled to the production of nanopatterned coatings on large-area substrates without compromising film homogeneity. The open pore structure of the nanopatterned surface prepared by the EISA technique enables selective functionalization of the continuous metal oxide network and the substrate with self-assembled monolayers (SAM).

In the thesis, wetting results on unfunctionalized and selectively hydrophobized nanopatterns were presented. The influence of the geometrical parameters (pore diameter, wall thickness, layer thickness) and hydrophilic-hydrophobic contrast on the nanometer length scale on the wetting properties of these materials were studied. The high homogeneity both in terms of the patterning as well as the thickness made it possible to experimentally determine the important parameters needed for the modeling of the wetting according to existing theories for the wetting of rough and heterogeneous surfaces. Superhydrophilicity was observed on unfunctionalized nanopatterns with Wenzel r-values between 1.7 and 2. The results could be modeled according to the theory of Bico et al., which suggests that the liquid droplet rests on a composite surface of solid and liquid. For the same nanopatterns, where the TiO_2 network was hydrophobized with a fluorinated organophosphonate (Zonyl), the wetting behavior was dependent on the type of water droplet deposition. For gently deposited small droplets, the measured static and advancing contact angles were higher than those for either of its constituents. The results could be modeled with the Cassie-Baxter equation, which assumes that air is trapped in the craters. When larger droplets were free-falling onto the surface, the measured contact angles were considerably smaller. These results fitted better to the Cassie-Wenzel theory, which assumes contact between the liquid and the surface. A large contact angle hysteresis was observed on the Zonyl-functionalized nanopatterns, which was ascribed to the continuity of the TiO_2 network. An important finding was that a layer thickness in the range of 5.5-11 nm had a significant effect on the wetting behavior.

Finally, the wettability of very thin nanopatterned layers of TiO_2 on SiO_2 was studied. The nanopatterns had *r*-values close to 1, and the hydrophilic-hydrophobic contrast was tuned with UV-photopatterning. A fluoroalkylsilane (FAS) was self-assembled onto the $TiO_2@SiO_2$ nanopattern, after which the film was exposed to UV irradiation. UV-photopatterning was possible because of the very different photocatalytic properties of TiO_2 and SiO_2. The FAS layer was decomposing quite fast on the TiO_2 part of the patterned surface, while FAS was stable for longer periods of time on the SiO_2 part. The hydrophilic-hydrophobic contrast was tuned by varying the length of UV irradiation time. The fraction of remaining FAS, f_{FAS} on the TiO_2@SiO_2 nanopattern was determined with XPS. f_{FAS} –values was also calculated from water contact angle measurements of the composite and corresponding reference samples, by using existing wetting models for heterogeneous surfaces. f_{FAS}–values determined from static water contact angle measurements gave the best agreement with the XPS results, while f_{FAS}–values calculated from advancing and receding contact angles overestimated and underestimated the XPS-derived f_{FAS}–values, respectively. The Cassie model gave a slightly better fit to the XPS data than the Israelachvili model.

The results presented in the thesis are believed to improve the understanding of the wettability of surfaces with heterogeneities on the nanometer length scale. This knowledge hopefully facilitates the fabrication of future devices within nanotechnology. Hydrophobically/hydrophilically nanopatterned surfaces are for instance promising materials for the manipulation of the flow of small volumes of liquid in the field of microfluidics.[2] Microfluidic devices have promising applications in bioassays, microreactors, and in chemical and biological sensing.[13]Future interesting work on nanopatterned ceramic surfaces could include the fabrication of hierarchically patterned surfaces. For example, by exposing a hydrophobized TiO_2@SiO_2 nanopattern to UV-light through a photomask, micrometer sized hydrophilic stripes or patches with nanosized hydrophobic islands could be prepared within an otherwise hydrophobic network. The flow of liquid on such materials could be controlled by the micropatterned structure, while some desired functionality of the material could be introduced by the nanosized islands.

10. ACKNOWLEDGEMENTS

First of all, I am deeply thankful to Professor Jarl. B. Rosenholm for in the first place giving me the opportunity to work at the Laboratory for Physical Chemistry, and for the patience you have had with me finishing this work. You introduced me to this intriguing field many years ago, and you encouraged me to continue with my PhD. This thesis would simply not have been possible without your contribution. Thank you.

I am forever grateful for the guidance and help from my supervisor Professor Mika Lindén. You have been very inspiring with your broad scientific knowledge, and your positive attitude has helped me to carry on this work especially during difficult times. I have also enjoyed our non-scientific activities, like grabbing a beer (or two) in the pub or playing music in the FyKe-band.

Professor Jouko Peltonen is thanked for the supervision in the beginning of my PhD, and for introducing me to the world of AFM.

This work would not have been possible without the help from many people. I would like to thank all of my co-authors for their valuable contributions. Dr. Sami Areva, Dr. Monica Kuemmel, Dr. Felix Brieler, and Qian Xu are acknowledged for the preparation of the surfaces studied in the thesis. Professor David Grosso is thanked for sharing his expertise in the field of thin films. Dr. Viljami Pore and Mikko Heikkilä are acknowledged for XRD measurements. I would also like to thank Lic. Jyrki Juhanoja at Top Analytica Ltd. for all his guidance with SEM and ESCA measurements.

Present and former coworkers at the Laboratory of Physical Chemistry are thanked for creating a pleasant atmosphere to work in. I would especially like to thank Dr. Jan-Henrik Smått for being a through friend and for all his support during my time in Åbo.

I would like to thank Dr. Rossen Sedev and Dr. Neil Shirtcliffe for reviewing the thesis and for valuable comments. Especially Rossen, who is traveling all the way from Australia to act as the opponent at the public defense of this thesis, is deeply acknowledged.

The Finnish Funding Agency for Technology and Innovation (TEKES), the Academy of Finland, the Graduate School of Materials Research (GSMR), and the integrated EU project (NanoEar) are all acknowledged for financial support.

My warmest gratitude goes to my family for all their support through the years.

Finally, I am deeply grateful to my girlfriend Helka for all her support and understanding.

Åbo, September 2010

Mikael Järn

11. REFERENCES

(1) Dorrer, C.; Ruehe, J. Some Thoughts on Superhydrophobic Wetting. *Soft Matter* **2009**, *5*, 51-61.

(2) Blossey, R. Self-Cleaning Surfaces - Virtual Realities. *Nature Materials* **2003**, *2*, 301-306.

(3) Barthlott, W.; Neinhuis, C. Purity of the Sacred Lotus, Or Escape from Contamination in Biological Surfaces. *Planta* **1997**, *202*, 1-8.

(4) Roach, P.; Shirtcliffe, N. J.; Newton, M. I. Progess in Superhydrophobic Surface Development. *Soft Matter* **2008**, *4*, 224-240.

(5) Feng, X.; Jiang, L. Design and Creation of superwetting/antiwetting Surfaces. *Adv Mater* **2006**, *18*, 3063-3078.

(6) Tahk, D.; Kim, T.; Yoon, H.; Choi, M.; Shin, K.; Suh, K. Y. Fabrication of Antireflection and Antifogging Polymer Sheet by Partial Photo Polymerization and Dry Etching. *Langmuir* **2010**, *26*, 2240-2243.

(7) Fujishima, A.; Honda, K. Electrochemical Photolysis of Water at a Semiconductor Electrode. *Nature* **1972**, *238*, 37-+.

(8) Miyauchi, M.; Nakajima, A.; Watanabe, T.; Hashimoto, K. Photocatalysis and Photoinduced Hydrophilicity of various Metal Oxide Thin Films. *Chemistry of Materials* **2002**, *14*, 2812-2816.

(9) Fox, M. A.; Dulay, M. T. Heterogeneous Photocatalysis. *Chem. Rev.* **1993**, *93*, 341-357.

(10) Hoffmann, M. R.; Martin, S. T.; Choi, W. Y.; Bahnemann, D. W. Environmental Applications of Semiconductor Photocatalysis. *Chem. Rev.* **1995**, *95*, 69-96.

(11) Areva, S. Sol-gel derived titania based ceramic thin films for implant coatings, Åbo Akademi University, Åbo, Finland, 2006.

(12) Amjad, Z., Ed.; In *Mineral scale formation and inhibition;* Plenum Press: New York, 1995; .

(13) Zhao, B.; Moore, J. S.; Beebe, D. J. Surface-Directed Liquid Flow Inside Microchannels. *Science* **2001**, *291*, 1023-1026.

(14) Whitesides, G. M. The Origins and the Future of Microfluidics. *Nature* **2006**, *442*, 368-373.

(15) Michel, R.; Reviakine, I.; Sutherland, D.; Fokas, C.; Csucs, G.; Danuser, G.; Spencer, N. D.; Textor, M. A Novel Approach to Produce Biologically Relevant Chemical Patterns at the Nanometer Scale: Selective Molecular Assembly

Patterning Combined with Colloidal Lithography. *Langmuir* **2002**, *18,* 8580-8586.

(16) Young, T. An Essay of the Cohesion of Fluids. *Philos. Trans. R. Soc. London* **1805**, *95*, 65-87.

(17) Marmur, A. Soft Contact: Measurement and Interpretation of Contact Angles. *Soft Matter* **2006**, *2*, 12-17.

(18) Extrand, C. W. Contact Angles and their Hysteresis as a Measure of Liquid-Solid Adhesion. *Langmuir* **2004**, *20,* 4017-4021.

(19) McHale, G.; Shirtcliffe, N. J.; Newton, M. I. Contact-Angle Hysteresis on Super-Hydrophobic Surfaces. *Langmuir* **2004**, *20,* 10146-10149.

(20) Gao, L.; McCarthy, T. J. Contact Angle Hysteresis Explained. *Langmuir* **2006**, *22*, 6234-6237.

(21) Wenzel, R. N. Resistance of Solid Surfaces to Wetting by Water. *Ind. Eng. Chem.* **1936**, *28*, 988-994.

(22) Cassie, A. B. D. Contact Angles. *Discuss. Faraday Soc.* **1948**, *3*, 11-16.

(23) Israelachvili, J. N.; Gee, M. L. Contact Angles on Chemically Heterogeneous Surfaces. *Langmuir* **1989**, *5*, 288-289.

(24) Bico, J.; Thiele, U.; Quere, D. Wetting of Textured Surfaces. *Colloids and Surfaces A-Physicochemical and Engineering Aspects* **2002**, *206*, 41-46.

(25) de Gennes, P. -.; Brochard-Wyart, F.; Quéré, D. In *Capillarity and wetting phenomena;* Springer: New York, 2004; .

(26) Cassie, A. B. D., Baxter, S Wettability of Porous Surfaces. *Trans. Faraday. Soc.* **1944**, *40*, 546-551.

(27) Oliver, J. F.; Huh, C.; Mason, S. G. Resistance to Spreading of Liquids by Sharp Edges. *J. Colloid Interface Sci.* **1977**, *59*, 568-581.

(28) Wapner, P. G.; Hoffman, W. P. Partial Wetting Phenomena on Nonplanar Surfaces and in Shaped Microchannels. *Langmuir* **2002**, *18*, 1225-1230.

(29) Bico, J.; Marzolin, C.; Quere, D. Pearl Drops. *Europhys. Lett.* **1999**, *47*, 220-226.

(30) Patankar, N. A. On the Modeling of Hydrophobic Contact Angles on Rough Surfaces. *Langmuir* **2003**, *19*, 1249-1253.

(31) Patankar, N. A. Transition between Superhydrophobic States on Rough Surfaces. *Langmuir* **2004**, *20*, 7097-7102.

(32) Barbieri, L.; Wagner, E.; Hoffmann, P. Water Wetting Transition Parameters of Perfluorinated Substrates with Periodically Distributed Flat-Top Microscale Obstacles. *Langmuir* **2007**, *23*, 1723-1734.

(33) Extrand, C. W. Contact Angles and Hysteresis on Surfaces with Chemically Heterogeneous Islands. *Langmuir* **2003**, *19*, 3793-3796.

(34) Gao, L.; McCarthy, T. J. How Wenzel and Cassie were Wrong. *Langmuir* **2007**, *23*, 3762-3765.

(35) Larsen, S. T.; Taboryski, R. A Cassie-Like Law using Triple Phase Boundary Line Fractions for Faceted Droplets on Chemically Heterogeneous Surfaces. *Langmuir* **2009**, *25*, 1282-1284.

(36) McHale, G. Cassie and Wenzel: Were they really so Wrong? *Langmuir* **2007**, *23*, 8200-8205.

(37) Nosonovsky, M. On the Range of Applicability of the Wenzel and Cassie Equations. *Langmuir* **2007**, *23*, 9919-9920.

(38) Nosonovsky, M. Multiscale Roughness and Stability of Superhydrophobic Biomimetic Interfaces. *Langmuir* **2007**, *23*, 3157-3161.

(39) Brandon, S.; Haimovich, N.; Yeger, E.; Marmur, A. Partial Wetting of Chemically Patterned Surfaces: The Effect of Drop Size. *J. Colloid Interface Sci.* **2003**, *263*, 237-243.

(40) Iliev, S. D.; Pesheva, N. C. Wetting Properties of Well-Structured Heterogeneous Substrates. *Langmuir* **2003**, *19*, 9923-9931.

(41) Marmur, A.; Bittoun, E. When Wenzel and Cassie are Right: Reconciling Local and Global Considerations. *Langmuir* **2009**, *25*, 1277-1281.

(42) Girifalco, L. A.; Good, R. J. A Theory for the Estimation of Surface and Interfacial Energies .1. Derivation and Application to Interfacial Tension. *J. Phys. Chem.* **1957**, *61*, 904-909.

(43) Good, R. J.; Girifalco, L. A. A Theory for Estimation of Surface and Interfacial Energies .3. Estimation of Surface Energies of Solids from Contact Angle Data. *J. Phys. Chem.* **1960**, *64*, 561-565.

(44) Owens, D. K.; Wendt, R. C. Estimation of Surface Free Energy of Polymers. *J Appl Polym Sci* **1969**, *13*, 1741-&.

(45) Wu, S.; Brzozows.Kj Surface Free Energy and Polarity of Organic Pigments. *J. Colloid Interface Sci.* **1971**, *37*, 686-&.

(46) Vanoss, C. J.; Chaudhury, M. K.; Good, R. J. Interfacial Lifshitz-van der Waals and Polar Interactions in Macroscopic Systems. *Chem. Rev.* **1988**, *88*, 927-941.

(47) Della Volpe, C.; Siboni, S. Some Reflections on Acid-Base Solid Surface Free Energy Theories. *J. Colloid Interface Sci.* **1997**, *195*, 121-136.

(48) Della Volpe, C.; Maniglio, D.; Brugnara, M.; Siboni, S.; Morra, M. The Solid Surface Free Energy Calculation **-** I. in Defense of the Multicomponent Approach. *J. Colloid Interface Sci.* **2004**, *271*, 434-453.

(49) Lee, L. H. Correlation between Lewis Acid-Base Surface Interaction Components and Linear Solvation Relationship Solvatochromic Alpha and Beta Parameters (Vol 12, Pg 1681, 1996). *Langmuir* **1996**, *12*, 5972-5972.

(50) Shen, Q. On the Choice of the acid/base Ratio of Water for Application to the Van Oss-Chaudhury-Good Combining Rules. *Langmuir* **2000**, *16*, 4394-4397.

(51) Hollander, A. On the Selection of Test Liquids for the Evaluation of Acid-Base Properties of Solid-Surfaces by Contact-Angle Goniometry. *J. Colloid Interface Sci.* **1995**, *169*, 493-496.

(52) Shalel-Levanon, S.; Marmur, A. Validity and Accuracy in Evaluating Surface Tension of Solids by Additive Approaches (Vol 262, Pg 489, 2003). *J. Colloid Interface Sci.* **2003**, *268*, 272-272.

(53) Menard, E.; Meitl, M. A.; Sun, Y.; Park, J.; Shir, D. J.; Nam, Y.; Jeon, S.; Rogers, J. A. Micro- and Nanopatterning Techniques for Organic Electronic and Optoelectronic Systems. *Chem. Rev.* **2007**, *107*, 1117-1160.

(54) Xia, Y. N.; Rogers, J. A.; Paul, K. E.; Whitesides, G. M. Unconventional Methods for Fabricating and Patterning Nanostructures. *Chem. Rev.* **1999**, *99*, 1823-1848.

(55) Geissler, M.; Xia, Y. N. Patterning: Principles and some New Developments. *Adv Mater* **2004**, *16*, 1249-1269.

(56) Kumar, A.; Whitesides, G. M. Features of Gold having Micrometer to Centimeter Dimensions can be Formed through a Combination of Stamping with an Elastomeric Stamp and an Alkanethiol Ink Followed by Chemical Etching. *Appl. Phys. Lett.* **1993**, *63*, 2002-2004.

(57) Kim, E.; Whitesides, G. M. Use of Minimal Free-Energy and Self-Assembly to Form Shapes. *Chemistry of Materials* **1995**, *7*, 1257-1264.

(58) Palacin, S.; Hidber, P. C.; Bourgoin, J. P.; Miramond, C.; Fermon, C.; Whitesides, G. M. Patterning with Magnetic Materials at the Micron Scale. *Chemistry of Materials* **1996**, *8*, 1316-1325.

(59) Drelich, J.; Miller, J. D.; Kumar, A.; Whitesides, G. M. Wetting Characteristics of Liquid-Drops at Heterogeneous Surfaces. *Colloids and Surfaces A-Physicochemical and Engineering Aspects* **1994**, *93*, 1-13.

(60) Drelich, J.; Wilbur, J. L.; Miller, J. D.; Whitesides, G. M. Contact Angles for Liquid Drops at a Model Heterogeneous Surface Consisting of Alternating and Parallel Hydrophobic Hydrophilic Strips. *Langmuir* **1996**, *12*, 1913-1922.

(61) Morita, M.; Koga, T.; Otsuka, H.; Takahara, A. Macroscopic-Wetting Anisotropy on the Line-Patterned Surface of Fluoroalkylsilane Monolayers. *Langmuir* **2005**, *21*, 911-918.

(62) Stevens, N.; Priest, C. I.; Sedev, R.; Ralston, J. Wettability of Photoresponsive Titanium Dioxide Surfaces. *Langmuir* **2003**, *19*, 3272-3275.

(63) Kanta, A.; Sedev, R.; Ralston, J. Preparation of Silica-on-Titania Patterns with a Wettability Contrast. *Langmuir* **2005**, *21*, 5790-5794.

(64) Priest, C.; Sedev, R.; Ralston, J. Asymmetric Wetting Hysteresis on Chemical Defects. *Phys. Rev. Lett.* **2007**, *99*, 026103.

(65) Piner, R. D.; Zhu, J.; Xu, F.; Hong, S. H.; Mirkin, C. A. "Dip-Pen" Nanolithography. *Science* **1999**, *283*, 661-663.

(66) Haidara, H.; Mougin, K.; Castelein, G.; Schultz, J. Lateral Self-Organization and Ordering at Nanoheterogeneous Surfaces. *Langmuir* **2000**, *16*, 9121-9124.

(67) Priest, C.; Stevens, N.; Sedev, R.; Skinner, W.; Ralston, J. Inferring Wettability of Heterogeneous Surfaces by ToF-SIMS. *J. Colloid Interface Sci.* **2008**, *320*, 563-568.

(68) Meli, M.; Lennox, R. B. The Wetting of Gold and Silicon Nanoscale Arrays. *Langmuir* **2007**, *23*, 1619-1622.

(69) Lundgren, M.; Allan, N. L.; Cosgrove, T. Modeling of Wetting: A Study of Nanowetting at Rough and Heterogeneous Surfaces. *Langmuir* **2007**, *23*, 1187-1194.

(70) Onda, T.; Shibuichi, S.; Satoh, N.; Tsujii, K. Super-Water-Repellent Fractal Surfaces. *Langmuir* **1996**, *12*, 2125-2127.

(71) Shirtcliffe, N. J.; McHale, G.; Newton, M. I.; Perry, C. C. Intrinsically Superhydrophobic Organosilica Sol-Gel Foams. *Langmuir* **2003**, *19*, 5626-5631.

(72) Han, J. T.; Xu, X. R.; Cho, K. W. Diverse Access to Artificial Superhydrophobic Surfaces using Block Copolymers. *Langmuir* **2005**, *21*, 6662-6665.

(73) Chen, W.; Fadeev, A. Y.; Hsieh, M. C.; Oner, D.; Youngblood, J.; McCarthy, T. J. Ultrahydrophobic and Ultralyophobic Surfaces: Some Comments and Examples. *Langmuir* **1999**, *15*, 3395-3399.

(74) Oner, D.; McCarthy, T. J. Ultrahydrophobic Surfaces. Effects of Topography Length Scales on Wettability. *Langmuir* **2000**, *16*, 7777-7782.

(75) Shirtcliffe, N. J.; McHale, G.; Newton, M. I.; Perry, C. C. Wetting and Wetting Transitions on Copper-Based Super-Hydrophobic Surfaces. *Langmuir* **2005**, *21*, 937-943.

(76) Lau, K. K. S.; Bico, J.; Teo, K. B. K.; Chhowalla, M.; Amaratunga, G. A. J.; Milne, W. I.; McKinley, G. H.; Gleason, K. K. Superhydrophobic Carbon Nanotube Forests. *Nano Letters* **2003**, *3*, 1701-1705.

(77) Gao, L. C.; McCarthy, T. J. The "Lotus Effect" Explained: Two Reasons Why Two Length Scales of Topography are Important. *Langmuir* **2006**, *22*, 2966-2967.

(78) Zhu, L. B.; Xiu, Y. H.; Xu, J. W.; Tamirisa, P. A.; Hess, D. W.; Wong, C. P. Superhydrophobicity on Two-Tier Rough Surfaces Fabricated by Controlled Growth of Aligned Carbon Nanotube Arrays Coated with Fluorocarbon. *Langmuir* **2005**, *21*, 11208-11212.

(79) Gao, L.; McCarthy, T. J. "Artificial Lotus Leaf" Prepared using a 1945 Patent and a Commercial Textile. *Langmuir* **2006**, *22*, 5998-6000.

(80) Gao, L.; McCarthy, T. J. A Perfectly Hydrophobic Surface (Theta(A)/theta(R)=180 degrees/180 Degrees). *J. Am. Chem. Soc.* **2006**, *128*, 9052-9053.

(81) Singh, R. P.; Gaur, S. S.; White, D. J.; Nancollas, G. H. Surface Effects in the Crystal-Growth of Calcium-Oxalate Monohydrate. *J. Colloid Interface Sci.* **1987**, *118*, 379-386.

(82) Wu, W. J.; Zhuang, H. Z.; Nancollas, G. H. Heterogeneous Nucleation of Calcium Phosphates on Solid Surfaces in Aqueous Solution. *J. Biomed. Mater. Res.* **1997**, *35*, 93-99.

(83) Tarasevich, B. J.; Chusuei, C. C.; Allara, D. L. Nucleation and Growth of Calcium Phosphate from Physiological Solutions Onto Self-Assembled Templates by a Solution-Formed Nucleus Mechanism. *J Phys Chem B* **2003**, *107*, 10367-10377.

(84) Koutsoukos, P. G.; Nancollas, G. H. The Mineralization of Collagen Invitro. *Colloids and Surfaces* **1987**, *28*, 95-108.

(85) Wu, W. J.; Nancollas, G. H. Kinetics of Nucleation and Crystal Growth of Hydroxyapatite and Fluorapatite on Titanium Oxide Surfaces. *Colloids and Surfaces B-Biointerfaces* **1997**, *10*, 87-94.

(86) Dalas, E.; Kallitsis, J. K.; Koutsoukos, P. G. Crystallization of Hydroxyapatite on Polymers. *Langmuir* **1991**, *7*, 1822-1826.

(87) Spanos, N.; Koutsoukos, P. G. Hydroxyapatite Precipitation on a Carboxylated Vinyl Chloride-Vinyl Acetate Copolymer. *J. Mater. Sci.* **2001**, *36*, 573-578.

(88) Combes, C.; Freche, M.; Rey, C.; Biscans, B. Heterogeneous Crystallization of Dicalcium Phosphate Dihydrate on Titanium Surfaces. *Journal of Materials Science-Materials in Medicine* **1999**, *10*, 231-237.

(89) Dalas, E.; Chrissanthopoulos, A. The Overgrowth of Hydroxyapatite on New Functionalized Polymers. *J. Cryst. Growth* **2003**, *255*, 163-169.

(90) Tanahashi, M.; Kokubo, T.; Matsuda, T. Quantitative Assessment of Apatite Formation Via a Biomimetic Method using Quartz Crystal Microbalance. *J. Biomed. Mater. Res.* **1996**, *31*, 243-249.

(91) Wen, H. B.; de Wijn, J. R.; van Blitterswijk, C. A.; de Groot, K. Incorporation of Bovine Serum Albumin in Calcium Phosphate Coating on Titanium. *J. Biomed. Mater. Res.* **1999**, *46*, 245-252.

(92) Kokubo, T. Apatite Formation on Surfaces of Ceramics, Metals and Polymers in Body Environment. *Acta Materialia* **1998**, *46*, 2519-2527.

(93) Nooney, M. G.; Campbell, A.; Murrell, T. S.; Lin, X. F.; Hossner, L. R.; Chusuei, C. C.; Goodman, D. W. Nucleation and Growth of Phosphate on Metal Oxide Thin Films. *Langmuir* **1998**, *14*, 2750-2755.

(94) Barrere, F.; Snel, M. M. E.; van Blitterswijk, C. A.; de Groot, K.; Layrolle, P. Nano-Scale Study of the Nucleation and Growth of Calcium Phosphate Coating on Titanium Implants. *Biomaterials* **2004**, *25*, 2901-2910.

(95) Viitala, R.; Jokinen, M.; Peltola, T.; Gunnelius, K.; Rosenholm, J. B. Surface Properties of in Vitro Bioactive and Non-Bioactive Sol-Gel Derived Materials. *Biomaterials* **2002**, *23*, 3073-3086.

(96) Wu, W. J.; Nancollas, G. H. Kinetics of Heterogeneous Nucleation of Calcium Phosphates on Anatase and Rutile Surfaces. *J. Colloid Interface Sci.* **1998**, *199*, 206-211.

(97) Jokinen, M.; Patsi, M.; Rahiala, H.; Peltola, T.; Ritala, M.; Rosenholm, J. B. Influence of Sol and Surface Properties on in Vitro Bioactivity of Sol-Gel-Derived TiO_2 and TiO_2-SiO_2 Films Deposited by Dip-Coating Method. *J. Biomed. Mater. Res.* **1998**, *42*, 295-302.

(98) Peltola, T.; Jokinen, M.; Rahiala, H.; Patsi, M.; Heikkila, J.; Kangasniemi, I.; Yli-Urpo, A. Effect of Aging Time of Sol on Structure and in Vitro Calcium Phosphate Formation of Sol-Gel-Derived Titania Films. *J. Biomed. Mater. Res.* **2000**, *51*, 200-208.

(99) Peltola, T.; Paldan, H.; Moritz, N.; Areva, S.; Korventausta, J.; Jokinen, M.; Narhi, T.; Happonen, R. P.; Yli-Urpo, A. Methods to Enhance Biomimetic Activity and Ability to Tissue Bonding of Sol-Gel-Derived Nanoporous Titania. *Bioceramics 14* **2002**, *218-2*, 207-211.

(100) Brinker, C. J., Scherer, G. W. In *Sol-Gel Science: The Physics and Chemistry of Sol-Gel processing;* Academic Press: San Diego, USA, 1990; .

(101) Kajihara, K.; Nakanishi, K.; Tanaka, K.; Hirao, K.; Soga, N. Preparation of Macroporous Titania Films by a Sol-Gel Dip-Coating Method from the System Containing Poly(Ethylene Glycol). *J Am Ceram Soc* **1998**, *81*, 2670-2676.

(102) Kajihara, K.; Yao, T. Macroporous Morphology of the Titania Films Prepared by a Sol-Gel Dip-Coating Method from the System Containing Poly(Ethylene Glycol). I. Effect of Humidity. *J. Sol Gel Sci. Technol.* **1998**, *12*, 185-192.

(103) Yang, H.; Coombs, N.; Sokolov, I.; Ozin, G. A. Free-Standing and Oriented Mesoporous Silica Films Grown at the Air-Water Interface. *Nature* **1996**, *381*, 589-592.

(104) Yang, H.; Kuperman, A.; Coombs, N.; MamicheAfara, S.; Ozin, G. A. Synthesis of Oriented Films of Mesoporous Silica on Mica. *Nature* **1996**, *379*, 703-705.

(105) Brinker, C. J.; Lu, Y. F.; Sellinger, A.; Fan, H. Y. Evaporation-Induced Self-Assembly: Nanostructures made Easy. *Adv Mater* **1999**, *11*, 579-+.

(106) Lu, Y. F.; Fan, H. Y.; Stump, A.; Ward, T. L.; Rieker, T.; Brinker, C. J. Aerosol-Assisted Self-Assembly of Mesostructured Spherical Nanoparticles. *Nature* **1999**, *398*, 223-226.

(107) Kresge, C. T.; Leonowicz, M. E.; Roth, W. J.; Vartuli, J. C.; Beck, J. S. Ordered Mesoporous Molecular-Sieves Synthesized by a Liquid-Crystal Template Mechanism. *Nature* **1992**, *359*, 710-712.

(108) Binning, G.; Rohrer, H.; Gerber, C.; Weibel, E. Surface Studies by Scanning Tunneling Microscopy. *Phys. Rev. Lett.* **1982**, *49*, 57-61.

(109) Binnig, G.; Quate, C. F.; Gerber, C. Atomic Force Microscope. *Phys. Rev. Lett.* **1986**, *56*, 930-933.

(110) Zhong, Q.; Inniss, D.; Kjoller, K.; Elings, V. B. Fractured Polymer Silica Fiber Surface Studied by Tapping Mode Atomic-Force Microscopy. *Surf. Sci.* **1993**, *290*, L688-L692.

(111) Image Metrology, the Scanning Probe Image Prosessor, SPIP^{TM}, User’s and Reference Guide Version 4.4. **2007**.

(112) Stout, K. J., Ed.; In *Development of methods for the characterisation of roughness in three dimensions;* Penton Press: London, 2000; .

(113) Flegler, S. L.; Heckman Jr, J. W.; Klomparens, K. L., Eds.; In *Scanning and Transmission Electron Microscopy, An Introduction;* Oxford University Press Inc.: New York, 1993; .

(114) Briggs, D.; Seah, M., Eds.; In *Practical Surface Analysis, Volume 1, Auger and X-ray Photoelectron Spectroscopy;* Wiley: 1994; .

(115) Kanta, A.; Sedev, R.; Ralston, J. Thermally- and Photoinduced Changes in the Water Wettability of Low-Surface-Area Silica and Titania. *Langmuir* **2005**, *21*, 2400-2407.

(116) Martra, G. Lewis Acid and Base Sites at the Surface of Microcrystalline TiO2 Anatase: Relationships between Surface Morphology and Chemical Behaviour. *Applied Catalysis A-General* **2000**, *200*, 275-285.

(117) Wu, W.; Nancollas, G. H. Nucleation and Crystal Growth of Octacalcium Phosphate on Titanium Oxide Surfaces. *Langmuir* **1997**, *13*, 861-865.

(118) Shi, J. M.; Ding, C. X.; Wu, Y. H. Biomimetic Apatite Layers on Plasma-Sprayed Titanium Coatings After Surface Modification. *Surf. Coat. Technol.* **2001**, *137*, 97-103.

(119) Nancolla.Gh; Tomazic, B. Growth of Calcium-Phosphate on Hydroxyapatite Crystals **-** Effect of Supersaturation and Ionic Medium. *J. Phys. Chem.* **1974**, *78*, 2218-2225.

(120) Iijima, M.; Tohda, H.; Moriwaki, Y. Growth and Structure of Lamellar Mixed-Crystals of Octacalcium Phosphate and Apatite in a Model System of Enamel Formation. *J. Cryst. Growth* **1992**, *116*, 319-326.

(121) D'Andrea, S. C.; Fadeev, A. Y. Covalent Surface Modification of Calcium Hydroxyapatite using n-Alkyl- and n-Fluoroalkylphosphonic Acids. *Langmuir* **2003**, *19*, 7904-7910.

(122) Dorrer, C.; Ruehe, J. Advancing and Receding Motion of Droplets on Ultrahydrophobic Post Surfaces. *Langmuir* **2006**, *22*, 7652-7657.

(123) Nosonovsky, M.; Bhushan, B. Biomimetic Superhydrophobic Surfaces: Multiscale Approach. *Nano Letters* **2007**, *7*, 2633-2637.

(124) Werner, O.; Wagberg, L.; Lindstrom, T. Wetting of Structured Hydrophobic Surfaces by Water Droplets. *Langmuir* **2005**, *21*, 12235-12243.

(125) Tatsuma, T.; Kubo, W.; Fujishima, A. Patterning of Solid Surfaces by Photocatalytic Lithography Based on the Remote Oxidation Effect of TiO_2. *Langmuir* **2002**, *18*, 9632-9634.

(126) Lee, J. P.; Kim, H. K.; Park, C. R.; Park, G.; Kwak, H. T.; Koo, S. M.; Sung, M. M. Photocatalytic Decomposition of Alkylsiloxane Self-Assembled Monolayers on Titanium Oxide Surfaces. *J Phys Chem B* **2003**, *107*, 8997-9002.

(127) Priest, C.; Albrecht, T. W. J.; Sedev, R.; Ralston, J. Asymmetric Wetting Hysteresis on Hydrophobic Microstructured Surfaces. *Langmuir* **2009**, *25*, 5655-5660.

(128) Fang, C. P.; Drelich, J. Theoretical Contact Angles on a Nano-Heterogeneous Surface Composed of Parallel Apolar and Polar Strips. *Langmuir* **2004**, *20*, 6679-6684.

(129) Anantharaju, N.; Panchagnula, M. V.; Vedantam, S. Asymmetric Wetting of Patterned Surfaces Composed of Intrinsically Hysteretic Materials. *Langmuir* **2009**, *25*, 7410-7415.

12. SAMMANFATTNING PÅ SVENSKA

Vätning av fasta ytor är ett viktigt fenomen i såväl naturen som i en lång rad av industriella tillämpningar. Det är allmänt känt att vätningen av en fast yta styrs av ytans kemi samt struktur. I avhandlingen studerades vätningsegenskaper hos titandioxid-baserade kerama ytor. Ytorna framställdes med hjälp av en sol-gel process, där substratet bestryks genom att doppas i en lösning innehållande titandioxidkällan, varefter den oorganiska strukturen stabiliseras genom kalcinering vid hög temperatur. I den första delen av avhandlingen studerades ytor med icke väldefinierad heterogenitet. Ytans topografi varierades genom att ändra på syntesparametrarna t.ex. kalcineringstemperaturen eller tillsättning av tillsatsämnen. Ytans egenskaper kunde beskrivas med hjälp av en serie ytråhetsparametrar, som erhölls från atomkraftsmikroskopimätningar (AFM). Resultaten visade att en ytas struktur inte i tillräcklig utsträckning kan beskrivas med den ofta använda RMS ytråhetsparametern, dvs. standardavvikelse på höjden, utan att även andra parametrar behövs för att beskriva fenomen som vätning och utfällning av oorganiskt material. Den kombinerade effekten av ytkemi samt ytstruktur på en ytas vätningsegenskaper studerades vidare genom tillverkning av superhydrofoba (vattenavstötande) material. Dessa ytor framställdes genom utfällning av kalciumfosfat på titandioxidfilmerna som därefter hydrofoberades med en fluorbaserad surfaktant. Ytans extrema vattenavstötande egenskaper kunde förklaras med kalciumfosfatets ytstruktur, som efter hydrofobering ledde till en minimal kontakt mellan vätskan och det fasta materialet.

I den andra delen av avhandlingen studerades väldefinierade ”nanomönstrade” ytor. Materialet bestod av tunna filmer av titandioxid, där substratet (kiseldioxid eller guld) var tillgängligt genom hexagonalt ordnade nanokratrar av storleken 10-50 nm. Dessa material var väl anpassade som modellytor för studier på hur heterogenitet på nanometernivå påverkar vätningsbeteendet, eftersom titandioxidnätverket och substratet selektivt kunde funktionaliseras med organiska molekyler. Effekten av ytans geometri (kraterdiameter, väggtjocklek, filmtjocklek) samt den hydrofila-hydrofoba kontrasten i materialet studerades. Resultaten kunde framgångsrikt modelleras med existerande teorier för vätning av heterogena ytor.

Åbo Akademi University

GSMR
Graduate School of Materials Research
funded by ACADEMY OF FINLAND AND THE MINISTRY OF EDUCATION

PRINTED INTELLIGENCE
FUN MAT
FUNCTIONAL MATERIALS

ISBN 978-952-12-2470-6

Painosalama Oy – Turku, Finland 2010